The Pennsylvania State University

The Graduate School

Department of Physics

CRYSTAL LATTICE OPTIMIZATION AND NEW FORMS OF SILICON

A Thesis in

Physics

by

David P. Stucke

Submitted in Partial Fulfillment
of the Requirements
for the Degree of

Doctor of Philosophy

May 2006

The thesis of David P. Stucke has been reviewed and approved * by the following:

Vincent Crespi
Professor of Physics
Thesis Adviser
Chair of Committee

Jainendra K. Jain
Professor of Physics

Jorge Sofo
Professor of Physics

Theresa Mayer
Professor of Electrical Engineering

Jayanth Banavar
Professor of Physics
Department Head

* Signatures are on file in the Graduate School.

Abstract

In Chapter 1 a basic outline of the two main methods used in this thesis is given. A genetic algorithm optimization method based on the concept of natural selection is given. The important factors to consider in creating an effective genetic algorithm search are described. I then give a brief overview of Density Functional Theory (DFT) which is the technique most commonly used to do ab-inito calculations on solid-state systems. The basis for its formulation along with how it is applied to a practical system with some approximations is discussed.

In Chapter 2 a description of a genetic search algorithm for optimizing the crystal structure of an infinite crystal is given. This method is applied to a system of colloidal spheres, where the packing density is the figure of merit for structure selection. Our examination of self-assembled multi-component crystals of nanoparticles predicts several new structures with stoichiometries of AB (fused spheres), ABC_2, ABC_3, ABC_4 and AB_2C_2. These new structures have hierarchical layered or linear arrangements that could be useful for functional self-assembled systems. For example, the fused-sphere binary crystal assembles with zig-zag rows of parallel nanowires. The genetic search suceeds while a comparable stochastic algorithm fails to find any structures better than the well-known unary or binary phase-separated systems. Here we describe the algorithm and the results it produces: several new classes of binary and ternary crystals of spherical nanoparticles, including a family of layered perovskite-like systems and an unusual three-dimensional array of parallel zig-zag nanowires.

In Chapter 3, We discuss the possibility of constructing new forms of silicon by building in multiple bonds consistent with molecules that have been produced experimentally. We find a dilated diamond crystal lattice containing a silicon-silicon triple bond that is metastable. This structure has very soft vibrational modes that are common in similar structures with buckled bonds (similar to quarts). The crystal may be stabilized by synthesizing in a rare gas environment, where a mixture of krypton and neon or helium may work best. Constructing a crystal lattice out of the trisilaallene central region leads to an unstable crystal structure. The main reason for this instability is due to the flexibility in the location of the sp-hybridized atom. Relaxing this structure leads to a new sp^2-sp^3 hybrid structure. There are a family of structures with ribbons of graphitic silicon held together by sp3 silicon atoms. The ribbon width can be increased to lead towards more graphitic silicon-like results. Graphitic silicon is predicted to be stabilized under negative pressure. Due to the similarity to graphitic silicon, we expect this family of structures may be stabilized in an environment of negative pressure as well..

Table of Contents

List of Tables

List of Figures

Acknowledgments

First, I would like to thank my wife, Sheri Stucke, for her support, encouragement, and understanding throughout this whole process.

I would like to thank my advisor, Vincent Crespi , for all of his guidance through the past 6 years. I appreciate all of his input and support through all the bugs and bumps along the way. Observing the way Vin approaches problems to put a unique spin on things is very enlightening. Vin really helps to keep physics fun. I am grateful to have worked in his group.

I would like thank my committee members for their input to help me improve this work.

I would like to thank all of my friends I met throughout my graduate study. Paul Lammert was very valuable, always being available to help with any physics or computer problems that have you stuck. Jason Stecklein, is a great friend and I enjoyed our many times studying together at Iowa State. I would also like to thank Elena (Roxana) Margine and Al Kolmogorov for their help and for making my time at Penn State more enjoyable.

I would also like to thank my parents, David and Georgette Stucke, for always being there for me and encouraging me. Mom and Dad have always done everything they could to help me achieve my goals, and I am grateful for that. Along with mmy parents, my grandfather, Louis Dougherty, was a very important influence in stressing the importance of education as I grew up. I always wanted him to be here for this, he greatly missed.

Most importantly, I want to acknowledge my wife Sheri for her love and support through this journey. She is an amazing person and I am very lucky to have her by my side. She has always believed in me and helped to push me through the tough times. I love her very much and can't imagine being without her. We make a great team and I look forward to many wonderful years in the journey ahead together...

Chapter 1

Background and Methods

1.1 Optimization Methods

1.1.1 Optimization Methods

The simplest type of optimization problem is a problem which consists of only one variable. These one-dimensional problems have the advantage that it is easy to define a region where a minima must exist. Smooth continuous functions are straight forward to find a local minima through the use of the function derivatives. Finding a minima in a problem with more degrees of freedom is much harder. Examining the case with two degrees of freedom is equivalent to trying to find the lowest point in a range of mountains. Higher dimensional problems become very complicated and much more difficult very quickly. Wolpert and Macready [63, 64], state: “all algorithms that search for an extremum of a cost function perform exactly the same, when averaged over all possible cost functions”. The idea is that any improvement in performance over a particular type of problem is compensated for by a decrease in performance over a different class of problems. This emphasizes the importance of choosing the algorithm that suits the problem at hands. Optimization problems are typically classified into either constrained optimization problem or unconstrained optimization problem. Constrained optimization problems have some limitations on the range of the input variables to the function that are allowed, while unconstrained problems do not. This is on of the things one must consider when choosing an optimization method. A brief description of a few common optimization methods will be given along with some of the advantages and disadvantages of each.

Clustering methods perform a local search from selective points in the search space. Points are chosen in an attempt to avoid finding the same local minima repeatedly. Clustering methods need an objective function that is computationally inexpensive to evaluate since many points must be sampled to identify the clusters that fall in the same local minima. Clustering methods are most useful for problems with a small number of degrees of freedom.

The downhill simplex method is a multi-dimensional optimization method which uses a geometrical figure (simplex). A simplex is a figure consisting of N+1 points in a N dimensional space and all of their interconnecting line segments (in 2-d a triangle would be a simplex). The downhill simplex method takes a series of steps that move a point of the simplex where the function is highest toward the opposite face toward a lower point [43]. The simplex method is typically not very efficient requiring a large number of function evaluations. It has the advantage that is easy to implement if you just need to get something working quickly.

Multi-Resolution Method is a method that is used when the surface searched is very noisy having many sharp local minima. The idea is to create a new function similar to the original that will have a smoother surface with all the major minima in similar locations[32]. The problem with this method is that there are typically many function evaluations necessary to generate the smoothed function surface and it is possible that the minimum is removed in the smoothing process. This method is commonly used when analyzing and comparing computer images.

Another commonly used method is a conjugate gradient method. A conjugate gradient method is a local optimization method designed to quickly find a nearby local minimum. The conjugate gradient method uses the function values in addition to the partial derivatives of the function to choose a direction to travel towards the local minimum. This method can be very efficient when the function being optimized is nearly quadratic and will take only a few steps to find the minimum. This method is quick to converge when near a local minimum since it can be approximated by a parabolic minimum. Far away from a minimum the conjugent gradient method can be very inefficient due to the non-quadratic nature of the function[43]. A Monte Carlo search method is a class of algorithms for simulating a physical system by using statistical sampling through the use of random numbers. Monte Carlo methods are different from the previous methods mentioned since Monte Carlo methods are not deterministic, being dependent on random numbers to generate adequate statistical sampling. All previous methods mentioned are deterministic and will find the same result given the same starting conditions. Simulated annealing is a type of a Monte Carlo method based on the physical process annealing. In an annealing process a material is heated to a high temperature and is slowly cooled to a frozen state at zero temperature. This slow process allows escaping from shallow local minima due to the remaining kinetic energy. Simulated annealing performs well in combinatorial problems with many discrete shallow local minima. In this thesis we choose a genetic algorithm optimization methods for our particular problem [43]. Due to the many local minima present and the complexity of the search space in this unconstrained optimization problem a genetic algorithm is a good choice to examine. We will discuss the genetic algorithm and its advantages and disadvantages in the following section.

1.1.2 Genetic Algorithm Optimization

Genetic algorithms first appeared in the late 1950's, used by evolutionary biologists who were seeking to model specific aspects of evolution. In 1962 several researchers independently developed evolution based algorithms for function optimization and machine learning [18]. These techniques involved one parent which was mutated to produce one offspring, and the better of the two was kept. Later versions introduced the idea of a population with mating (crossover) and mutation [59, 27]. This technique was mainly used in computer science and biology for optimization of complex systems with a large configuration space and in genetic programming. Genetic programming is defined as self-evolving program designed to optimize the performance of the program in a particular task. Genetic algorithms have been applied in many different problems such as scheduling problems, game theory and electronic circuit design [27]. In 1995, Deaven and Ho [7] implemented the idea of a genetic algorithm search to optimize the molecular geometry of atomic clusters. The algorithm found the optimal structure for various atomic clusters including the 60 carbon atom case finding the buckyball as the optimal solution. The genetic algorithm performed better than simulated annealing, which was the most commonly used method. In addition to carbon clusters, this algorithm has also been successful in finding improved structures for medium sized ($n < 13$) silicon structures using LDA to evaluate the energy[16]. This method also solved the optimal locations for charged particles restricted to the surface of a sphere as well. We show how the genetic algorithm can be applied to an infinite crystal system and find several new and interesting structures.

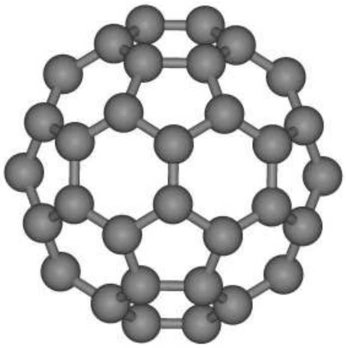

Fig. 1.1. Buckminster Fullerine (a.k.a. Buckyball) solved as the lowest energy structure for a C_{60} cluster using a the hybrid genetic algorithm of Deaven and Ho.

Genetic searches are so called since they borrow from biology the idea of creating new “child” structures by combining characteristics (i.e. genes) from “parent” structures. In our case, the structures are parameterized by various displacement vectors (defined below) and vectors from each parent are combined to construct a child. A genetic search takes long strides in configuration space. Therefore the algorithm will work best if the surface defined by the figure of merit (such as a binding energy or packing density) has long valleys oriented along coordinate directions. Geometrically, the merging of structural information from two parent structures into a child, (within an M dimensional configuration space), corresponds to finding the single point of intersection between

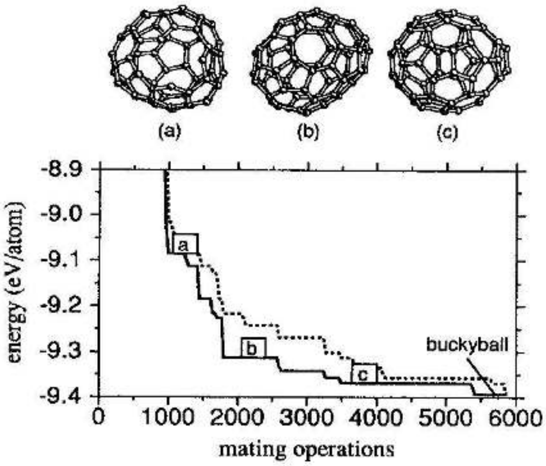

Fig. 1.2. Energy versus number of mating operations for a C_{60} cluster. The solid line is the lowest energy structure (population size=4) and the dotted line is the highest energy structure. Intermediate structures are shown at (a), (b) and (c). [7]

one m and one $M - m$ dimensional hyperplane, each passing through one parent. If coordinate directions define valleys, then the child has a better probability of sitting near the intersection of two valleys; a subsequent local optimization can then fine-tune the structure before the next generation.

The genetic algorithm begins with an initial population of creatures. The initial population is typically a randomly generated group of solutions to the problem being examined. Parent creatures are chosen from this population either randomly or with some fitness based selection process. The parents mate to form children maintaining some of the characteristics from each of the parents. Some random mutations are introduced during this mating (crossover) process. The children are then inserted into the population, typically replacing the least-fit creatures in the population. This procedure is repeated until a stopping criterion is met. The stopping criterion could be a preset number of generations or some condition on the fitness parameter. Figure 1.3 shows a flow chart depicting the method of the genetic algorithm [59].

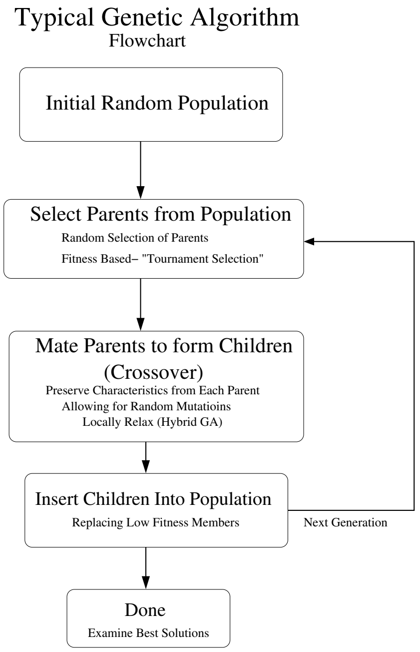

Fig. 1.3. Flowchart for a typical Genetic Algorithm.

The genetic algorithm is an effective method when there is a large configuration space with many local optima. Success of the GA requires certain topographical features in the fitness surface, so that characteristics that are good in the parents are also good in the children, in a new context. In order to avoid being trapped in a local minimum, mutation is an important part of the mating process. While mutations rarely improve the overall fitness of a child, it allows children to escape a local minimum by travelling a small distance in some random direction in configuration space. A large complex configuration

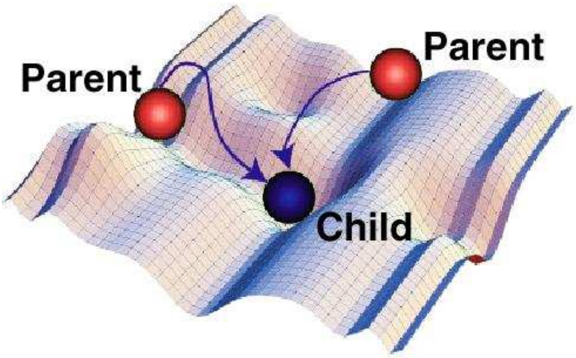

Fig. 1.4. Configuration space representation of the mating process (crossover). Recombination of two different parent structures represented in a way to preferentially move along valleys in the multidimensional configuration space.

space is not the only requirement for a problem that may be approached with a genetic algorithm. The main obstacle to implementing an effective genetic algorithm search is a useful representation of a solution to your problem. A solution to the problem should be represented in a way that the “genes” carried forward in the mating (crossover) procedure represent as many of the important features of the solution as possible. In addition there should be a well definable “fitness” measure for each configuration in the search space. For certain problems it may not be clear how to define a function that outputs the fitness of a structure.

The mating procedure for the genetic algorithm implementation for atomic cluster optimization involved cutting one cluster in two by some randomly placed plane. Similarly the other parent cluster is cut by the same plane. The plane is then shifted to maintain the correct number of atoms in the child after recombining portions from each parent. In this case the “genes” are the cartesian coordinates of each atom in the cluster.

The mating procedure preserves the local bond distances and bond angles within each half of the cluster, allowing some of the good characteristics of the parent to be carried forward to the child. The implementation of the genetic algorithm of Deaven and Ho was a hybrid genetic algorithm. The children are optimized with a standard conjugate gradient relaxation to more quickly find the local minimum. After the local relaxation the children are inserted into the population. In the case of atomic cluster optimization there is not a problem defining a fitness function. The energy of the structure is used as the fitness function.

In nature, reproduction of two parents involves half of the chromosomes from each parent to create the chromosomes for the child. We use this as a guide, but we have added flexibility that may potentially aid the search algorithm for particular problem types. We are not required to carry forward exactly half of the genes from each parent to the child. The most commonly used crossover method is a one-point crossover. In a one-point crossover, a gene sequence is cut at some random point in the sequence. Every gene before the cut in one parent carries forward to the child and every gene after the cut carries forward from the other parent. Sinlge-point crossover is one example where a larger portion of genes from one parent may proceed to the child. Two-point crossover is done in the same way, except the gene sequence is cut in two places, with alternating portions carrying forward to the child from each parent. Uniform crossover is also sometimes used. Uniform crossover, allows each gene to be randomly chosen from one of the parents to be carried forward in the child. Depending on the fitness landscape and the parametrization of the problem one of these methods may outperform the others. A uniform crossover method will perform well when each gene has enough internal structure to sufficiently represent an important feature of the problem. In our case of infinite crystal optimization we used a single-point crossover. The single-point crossover method will carry forward more important features to the children since in our parametrization contiguous genes are preferred to preserve additional bond angles.

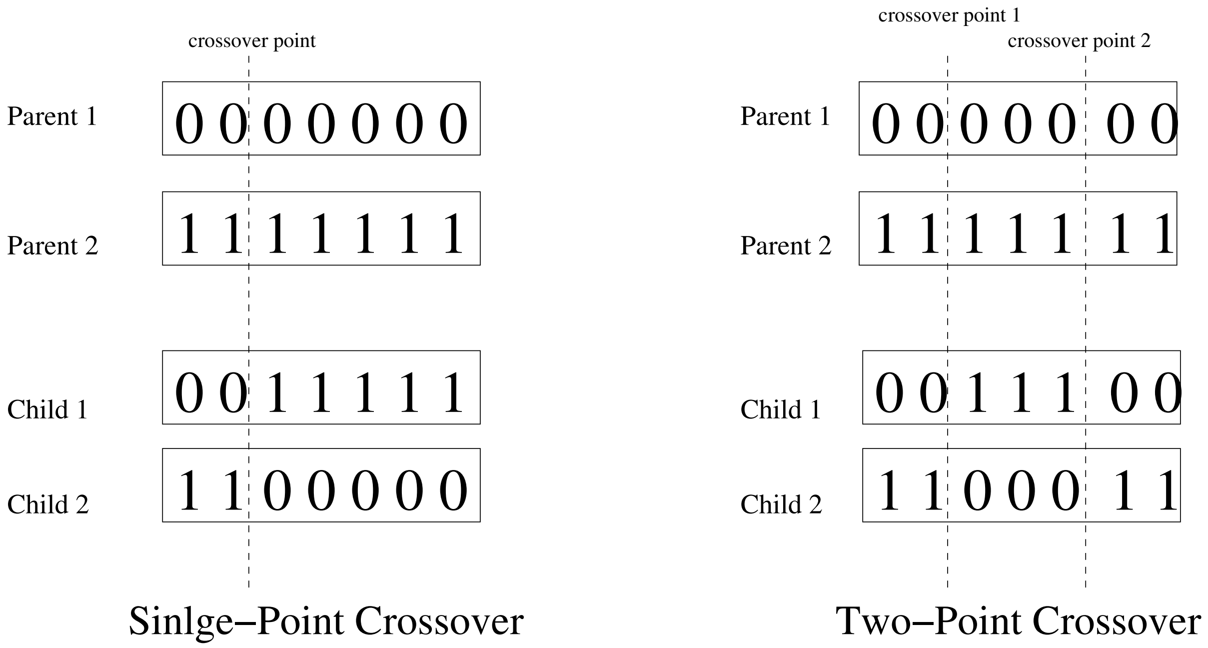

Sinlge–Point Crossover

Two–Point Crossover

Fig. 1.5. Depiction of one-point and two-point crossover methods.

One well known problem that does occur with a genetic algorithm is a premature convergence of the population. In biology this problem also occurs and is known as genetic drift. We combat this cloning problem in the genetic algorithm by resticting the children that are allowed to be inserted into the population. We use a similarity inner product (defined in Chapter 2) along with requiring a minimum δE for each child from all others currently in the population. Using this procedure suppresses genetic cloning and helps to prevent the population getting stuck in a local minimum.

One of the major advantages of a genetic algorithm is that it typically performs well in landscapes that are discontinuous or noisy, due to the ability to efficiently explore a large landscape. A genetic algorithm is an inherently parallel process. Each creature in the population can reproduce and evolve separately from others in the population without depending on the other members of the population. This is a very positive aspect of the genetic algorithm for attacking large configuration spaces through the use of parallel computers. The speed of the search increases approximately proportional to the number of processors used in the search. Since members of the population can be evaluated individually and inserted into the population as individual processors complete each evaluation.

For certain problems finding the absolute best solution to a problem may not be necessary. Finding a solution to the problem that is better than what is currently known may be sufficient or there may be many solutions to a problem with a similar fitness values where it is unrealistic to exhaustively search the many similar solutions. Problems of this type are ideal for the genetic algorithm, it can very quickly search a complicated fitness landscape to find reasonable solutions to the problem. In a typical global optimization problem, you do not know when you have reached the best global solution to a problem. Comparing your best solution to the solution currently used is all that is necessary.

1.2 Density Functional Theory

1.2.1 Density Functional formalism: Hohenberg-Kohn theorems

A central problem of quantum mechanics is to solve for the wavefunction of N interacting particles. The wavefunction completely describes the system and allows us to calculate any information desired about the system. The Schrödinger equation allows us to solve for the wavefunction for a system given the interactions between particles. The Schrödinger equation is given as:

$$\hat{H}\Psi(r_i,..,r_n,R_1..,R_N) = E\Psi(r_i,..,r_n,R_1,..R_N) \tag{1.1}$$

$$\begin{aligned}\hat{H} &= \sum_i -\frac{1}{2}\nabla_i^2 + \sum_i -\frac{1}{2M_i}\nabla_i^2 + \frac{1}{2}\sum_{i\neq j}\frac{1}{|r_i - r_j|} \\ &+ \frac{1}{2}\sum_{i\neq j}\frac{Q_iQ_j}{|R_i - R_j|} - \sum_{i\neq j}\frac{Q_j}{|r_i - R_j|}\end{aligned}$$

,where r, and R indicate the position operators acting on the electrons and nuclei respectively. M_i and Q_i are the mass and charge of the nuclei. The electron charge, mass and $\hbar$ are equal to one in these units. In order to make this problem computationally more tractable, we may use the Born Oppenheimer approximation. The Born Oppenheimer approximation comes from the fact that the mass of the electrons is much smaller than the mass of the nuclei. Using this, a reasonable approximation is to decouple the electronic and nuclear parts of the wavefunction since the typical velocities of the electrons are much larger than those nuclei. We can further simplify the problem by treating the nuclei as classical particles where their position operators can be treated as position variables. This leaves all the quantum effects contained in the electronic wavefunctions in a simpler Hamiltonian. We need to solve the Schrödinger equation with the following Hamiltonian:

$$\hat{H}^{el} = \sum_i -\frac{1}{2}\nabla_i^2 + \frac{1}{2}\sum_{i \neq j} \frac{1}{|r_i - r_j|} + \sum_i V_{ext}(r_i) = \hat{T} + \hat{V}_{coulomb} + \hat{V}_{ext}, \tag{1.2}$$

where V_{ext} is the external potential due to the nuclei. The wavefunctions ψ are required to be antisymmetric under exchange of spatial an spin coordinates due to the Pauli exclusion principle. The solution to this problem is very difficult, due to the large number of degrees of freedom.

Hohenberg and Kohn approached this problem by noting that the ground-state density of a bound system of interacting electrons in some external potential determines the potential uniquely to within an additive constant[17]. The external potential and any physical property of a system is a unique functional of the electron ground state density. This theorem was proved by Hohenberg and Kohn in a relatively short and simple way. If we assume two different external potentials v_1 and v_2 that differ by more than a constant, and calculate the ground state energies of their corresponding Hamiltonians ($\hat{H}_1$ and $\hat{H}_2$) we have:

$$\begin{aligned} E_0|\psi_1\rangle &= \hat{H}_1|\psi_1\rangle = (\hat{T} + \hat{V}_{coulomb} + \hat{v}_1)|\psi_1\rangle \qquad (1.3) \\ E_0'|\psi_2\rangle &= \hat{H}_2|\psi_2\rangle = (\hat{T} + \hat{V}_{coulomb} + \hat{v}_2)|\psi_2\rangle \end{aligned}$$

If we suppose ψ_1=ψ_2, subtracting these equations from each other leads us to:

$$(\hat{v}_1 - \hat{v}_2)\psi_1 = (E_0 - E_0^{'})\psi_1 \tag{1.4}$$

$$(\hat{v}_1 - \hat{v}_2 - (E_0 - E_0^{'}))\psi_1 = 0$$

$$\hat{v}_1 - \hat{v}_2 = (E_0 - E_0^{'}) = constant$$

Therefore, if ψ_1=ψ_2 then $\hat{v}_1$=$\hat{v}_2$ to within a constant [23]. According to the Hohenberg-Kohn theorem ρ determines the external potential v_{ext}. If we assume that two ground state both have the same density ρ_0 and $\psi_1 \neq \psi_2$, with ground state energy E_0 and $E_0^{'}$. Consider the following:

$$E_0 < \langle\psi_2|\hat{H}_1|\psi_2\rangle = \langle\psi_2|\hat{H}_2|\psi_2\rangle + \langle\psi_2|(\hat{H}_1 - \hat{H}_2)|\psi_2\rangle \tag{1.5}$$

$$= E_0^{'} - \int \rho_0(r)(V_{ext}^{'}(r) - V_{ext}(r)) \tag{1.6}$$

Using ψ_1 as the test function for $\hat{H}_2$ leads us to:

$$E_0^{'} < \langle\psi_1|\hat{H}_2|\psi_1\rangle = \langle\psi_1|\hat{H}_1|\psi_1\rangle + \langle\psi_1|(\hat{H}_2 - \hat{H}_1)|\psi_1\rangle \tag{1.7}$$

$$= E_0 - \int \rho_0(r)(V_{ext}(r) - V_{ext}^{'}(r)) \tag{1.8}$$

Adding these two equations results in:

$$E_0 + E_0^{'} < E_0 + E_0^{'} \tag{1.9}$$

This is a contradiction and thus the ground state density determines the external potential.

The energy can be written in terms of the external potential as:

$$E[\rho(r)] = \int \rho(r) v_{ext}(r) dr + F_{HK}[\rho(r)] \tag{1.10}$$

where $F_{HK}[\rho(r)]$ is an unknown functional (Hohenberg-Kohn functional) of the electron density only. A functional acts like a function that has a function as its argument instead of a variable and maps a function to a number like a function maps a numbr to a number. Using equation 1.2 above we can see that the Hohenberg-Kohn functional can be written as:

$$F_{HK}[\rho(r)] = \langle \psi | \hat{T} + \hat{V}_{coulomb} | \psi \rangle \tag{1.11}$$

The Hohenberg-Kohn functional above is not dependent on the specifics of the system. The Hamiltonian is completely defined by the external potential and the number of electrons. The second theorem of Hohenberg and Kohn states that the ground state energy can be obtained variationally and that the density the minimizes the total energy is the exact ground state density. This follows from the variational principle and the first Hohenberg-Kohn theorem. The Hohenberg-Kohn theorems prove existence of a unique density for non-degenerate ground state systems, but do not provide a systematic method for calculating the electronic density in practice [17].

Kohn and Sham replaced the system of interacting particles with a system of fictitious non-interacting particles with an effective Kohn-Sham single particle potential. This method is designed provide the same ground state electron density of the original interacting system and therefore gives exact results. From the Hohenberg-Kohnn theorem we know that the ground state density of an electronic system can be found by minimizing the energy functional while holding the number of electrons constant as the constraint as given below:

$$\delta\left[F_{HK}[\rho(r)]+\int V_{ext}(r)\rho(r)dr-\mu(\int\rho(r)dr-N)\right]=0, \tag{1.12}$$

where μ is the Lagrange multiplier associated with the constraint of a constant number of electrons (N). A non-interacting system can be separated into a set of single particle wavefunctions. We need to solve a Slater determinant of single particle wavefunctions to determine the many body-wavefunction.[52]:

$$\psi(r_1,...,r_N)=\Theta_S=\frac{1}{\sqrt{N!}}\begin{vmatrix}\phi_1(\mathbf{r}_1) & \phi_2(\mathbf{r}_1) & ... & \phi_N(\mathbf{r}_1)\\ \phi_1(\mathbf{r}_2) & \phi_2(\mathbf{r}_2) & ... & \phi_N(\mathbf{r}_2)\\ \vdots & \vdots & & \vdots\\ \phi_1(\mathbf{r}_N) & \phi_2(\mathbf{r}_N) & ... & \phi_N(\mathbf{r}_N)\end{vmatrix},$$

where ϕ_i are the single particle non-interacting wavefunctions.

The single particle Kohn-Sham operator is defined as:

$$\hat{H}_{KS}=-\frac{1}{2}\nabla^2+\hat{V}_S \tag{1.13}$$

Next we need to choose the $\hat{H}_{KS}$ such that the total electron density from all of the single particle Kohn-Sham orbitals (ϕ_i) give the exact ground state density of our system of interest. We need:

$$\rho_s(r) = \sum_i^N |\phi_i(r)|^2 = \rho_0(r), \tag{1.14}$$

where ρ_0 is the exact charge density of the real system of interacting particles that we are interested in. Kohn and Sham recommended separating the $F_{HK}[\rho(r)]$ functional as:

$$F_{HK}[\rho] = T_s[\rho] + J[\rho] + E_{xc}[\rho] \tag{1.15}$$

where $T_s[\rho]$ is sum of single particle kinetic energies from the Kohn-Sham orbitals and $J[\rho]$ is the Hartree term evaluating (Coulomb) energy. The kinetic energy of a non-interaction electron gas given as:

$$T_s[\rho(r)] = -\frac{1}{2}\sum_i^N \langle \phi_i | \nabla^2 | \phi_i \rangle \tag{1.16}$$

The Hartree term is $J[\rho]$ defined as:

$$J[\rho(r)] = \frac{1}{2}\int\int \frac{\rho(r)\rho(r')}{|r-r'|} \tag{1.17}$$

and using equation 1.10 the exchange-correlation energy term is defined as:

$$E_{xc} = E[\rho(r)] - (T_s[\rho(r)] + J[\rho(r)]) \tag{1.18}$$

The Kohn-Sham potential V_{ks} is defined as:

$$V_{ks}(r) = \int \frac{\rho(r')}{|r - r'|} dr' + V_{xc}(r) + V_{ext}(r) \tag{1.19}$$

, where the the exchange correlation potential is:

$$V_{xc}(r) = \frac{\delta E_{xc}[\rho]}{\delta \rho(r)} \tag{1.20}$$

The logic in separating the energy functional in this way is to break it into pieces that are well known and easier to calculate which will provide a reasonable first approximation to the energy functional. All of the unknown parts are then grouped together into the exchange correlation part. The exchange-correlation term contains all of the important physics about the interactions in the system. It contains information to add a correction to the non-interacting kinetic energy term above (T_s) in addition to all other electron-electron correlations that are unknown. The big problem in making density functional theory useful is determining the exchange-correlation functional. We need to make approximations to the (E_{xc}) exchange correlation term. Although in theory this method can produce exact results, we do not know the form of E_{xc}, and can not exactly calculate properties of the system due to this problem. Depending on the specific system the exchange correlation term will typically be small relative to the other terms. We need to approximate this functional. Some methods for approximating this function are discussed below. Electron spin can also be incorporated into DFT by separating the density into the sum of spin up and spin down densities.

1.2.2 Density Functional formalism: Local Density Approximation and Generalized Gradient Approximation

The Kohn-Sham approach provides a clever method for separating the energy into several parts, all of which are straightforward to calculate with the exception of the exchange-correlation functional (E_{xc}). Kohn and Sham began by assuming a slowly varying charge density and approximated the exchange-correlation functional as:

$$E_{xc}[\rho(r)] = \int \rho(r)\epsilon_{xc}(\rho(r))dr \tag{1.21}$$

,where ϵ_{xc} is the exchange-correlation energy per electron of a uniform electron gas with a density $\rho(r)$ [26]. This expression can be generalized as a Taylor series expansion of E_{xc} with equation 1.21 as the leading term in the expansion. Therefore, in the case with slowly varying charge densities the form in equation 1.21 is exact. Kohn and Sham expanded the charged density in terms of the non-interacting Kohn-Sham orbital wavefunctions and applied the variational principle to calculate as set of single-particle non-interacting Schrödinger equations. These equations are known as the Kohn-Sham equations and are given as:

$$\left(-\frac{1}{2}\nabla^2 + \int \frac{\rho(r')}{|r-r'|}dr' + V_{xc}(r)\right)\phi_i(r) = \epsilon_i\phi_i(r) \tag{1.22}$$

,where V_{xc} is given as:

$$V_{xc}(r) = \frac{d(\rho(r)\epsilon_{xc}(\rho(r)))}{d\rho}. \tag{1.23}$$

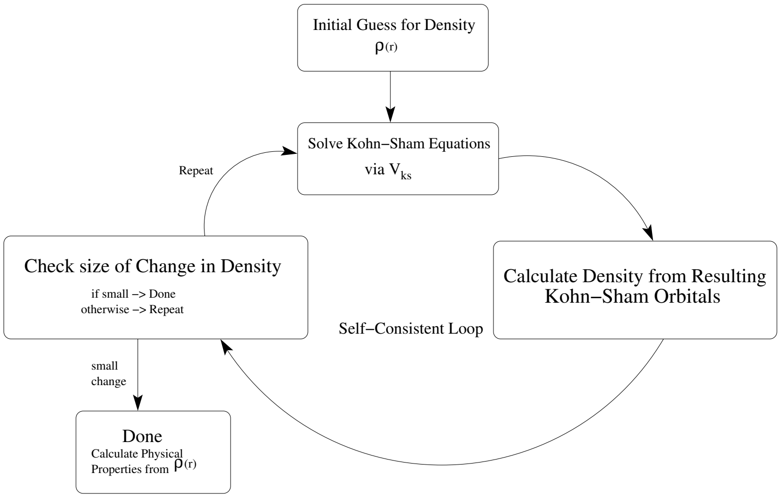

Fig. 1.6. Illustration of Self-Consistent Iteration Method for solving the Kohn-Sham equations for $\rho(r)$.

The Kohn-Sham equations (1.22) need to be solved using a self-consistent method. An initial guess is made for the density ($\rho(r)$). The resulting Kohn-Sham equations are solved for the Kohn-Sham orbitals ($\phi_i(r)$). These Kohn-Sham orbitals are then used to calculate the density (1.14). This new density is inserted into the Kohn-Sham equations and this process is repeated until the density change below some threshold. The single particle wavefunctions $\phi_i(r)$ do not correspond to electronic states of our interacting system. They represent the eigenstates for our fictitious non-interacting system as a method for us to determine the electron density $\rho(r)$ which allows us to calculate all needed physical properties of our ground state by the Hohenberg-Kohn theorem. Surprizingly, the energy level solutions of the Kohn-Sham equations in the local density approximation give reasonable results to systems that are very inhomogeneous. This local density function only depends on the electron density at a single point and contains no information about neighboring points. This local density approximation has been widely used for variety of systems. LDA is often used to calculate electronic band structures, even though these systems are far from homogeneous. The local density approximation (LDA) has several well-known problems. LDA fails to properly describe van der Waals forces since they depend on the charge density at another point (i.e. non-local effect). Incorporating non-local effects can be very challenging and computationally intractable due to the dependence of the charge density at one point to the charge density at all (or many other) points. Although LDA underestimates band gaps in semiconductors, it is not technically a failure of the method, since we are applying a ground state theory to excited states.

The most obvious extension to improve LDA is to include more terms in the expansion for the density. Allowing the energy to depend on the gradient of the charge density at a point as well. This type of approximation is know as a generalized gradient approximation (GGA) and is a "semi-local" method. GGA is known as a semi-local method since it still depends only on the charge density at a single point and its gradient at that point, the rate of change of the charge density at that point accounts for some longer distance effect. This method leads to an exchange correlation functional given as:

$$E_{xc}^{GGA}[\rho(r)] = \int \epsilon_{xc}[\rho(r)]\rho(r)dr + \int F_{xc}[\rho(r), |\nabla\rho(r)|]dr, \tag{1.24}$$

where ϵ_{xc} and F_{xc} need to be approximated. One popular method for parametrizing these functionals was proposed by Perdew and Wang (PW91) [42]. Perdew, Burke and Wang simplify this approximation by using a spherical averaging method for the density (PBE) [41]. Both of these methods are non-empirical and perform well for a wide variety of systems without any prior knowledge about the specifics of the system. Not all types of GGA methods are perform better than LDA consistently. Generally the PBE GGA method contains LDA and retains all of its good features, while providing an improved description of the relative stability of different phases. GGA softens bonds correcting for the over binding present in LDA [37, 9].

Chapter 2

Genetic Algorithm Optimization of Periodic Structures

2.1 Motivation

As increasing attention focuses on structuring materials on the nanometer scale, self-assembly techniques become more prominent. Whereas extended assemblies of monodisperse hard-core spheres form only close-packed lattices, more complex systems containing mixed or fused spheres, layered materials, ellipsoids, rods, or other structures promise a richer panoply of structural types, particularly when building blocks of different sizes are combined [8, 21, 22, 35, 57, 65, 67, 68, 69]. An efficient search algorithm for more complex periodic structures could therefore provide an important tool in the design of complex self-assembled materials. Theoretical guidance towards self-assembly requires a means to efficiently search the very large configuration spaces of extended systems for thermodynamically preferred structures.

The genetic algorithm was first applied to optimize cluster geometries in 1995 by Deaven and Ho [7]. The algorithm was demonstrated to be more efficient than simulated annealing to find the lowest energy structure for a cluster of 60 carbon atoms. A plane randomly cut the cluster into two pieces. Using the same plane for two parents does not guarantee that the total number of atoms will be conserved when recombining parts. To get around this problem Deaven and Ho cut one parent into two. The other parent has the plane is shifted to increase or decrease the number of atoms in order to keep the total number of atoms constant throughout the optimization. The central part to making the search successful was in the crossover procedure used. The genes used for this system were the cartesian coordinates of each atom. As mentioned in chapter 1, some of the important characteristics of the parents must be carried forward for the genetic algorithm to be useful. In this case, the local bond distances and bond lengths in each portion are conserved allowing for bonding motifs to be carried forward to the child structures. In an infinite crystal, the simple scheme of dividing the structure in half will not work. We provide a representation in which we can effectively divide the infinite crystal in half to maintain positive characteristics of the original structure.

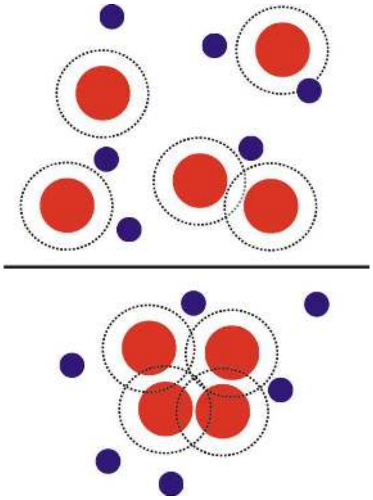

Fig. 2.1. Depletion Force Illustration: A binary mixture of hard spheres is depicted with a “forbidden region” outside the larger spheres, that is inaccessible to the center of the smaller spheres. As larger spheres approach then the forbidden region for the smaller spheres is reduced. This increases entropy of the system by adding to the accessible states for the smaller spheres causing a net attraction between the larger spheres, known as the depletion force.

2.2 Colloidal Crystals: Maximize Free Volume

Colloidal crystals have a wide interest due vast possible range of application to creating regular structures on a small scale. Many new types of colloidal particles and colloidal crystals are being produced. Colloidal crystals can be made from hard spheres, charged particles, or magnetic particles. In addition particle types are constantly expanding from hard spherical particles to composite sphere particles, “Ice cream cone” particles, patchy particles and elliptical particles[56, 33, 70]. We begin by considering a system of colloidal hard spheres. Colloidal hard sphere mixtures suspended in a fluid can spontaneously crystallize to form a variety of crystal structures. Entropy is the driving force for this disorder to order transition. Increased entropy prefers disorder, which seems against the formation of these colloidal crystals. Examining the case of two species of spheres as in figure 2.1 it is easy to see how entropy can drive the crystallization of the colloidal particles. Consider a region outside the larger particles (depicted with the dashed outline) that is inaccessible to the centers of the smaller particles. As two larger spheres approach each other these regions overlap, increasing the overall volume available to the smaller spheres. This increased volume available to the small spheres increases the entropy of the system since there are more configurations available to the smaller spheres. The number of smaller spheres entering the forbidden region becomes smaller increasing the overall entropy and this “depletion force” attracts the larger spheres together to maximize the available volume to the smaller particles. A system with a single type of sphere in a fluid packs with the same argument considering the fluid as smaller particles. Maximizing the free volume in this system is equivalent to maximizing the packing fraction of the system. We will use the packing fraction as our fitness measure in examining these colloidal systems as a way to optimize this entropy dominated regime.

2.3 Binary Mixtures and Experimental Progress

A significant amount of effort has been put into experimentally producing new self assembled crystal structures on a nanometer scale. The simplest method for estimating the regime of stability for a structure is to compare its packing fraction to the packing fraction of all other phase separated possibilities. Given in figure 2.2 a plot of the packing fraction of three different stoichiometries of binary sphere mixtures as a function of their size ratio. The region of stability predicted by packing fraction considerations is shown in grey. Using a more complicated cell-theory method [6], slightly different regions of stability are predicted.

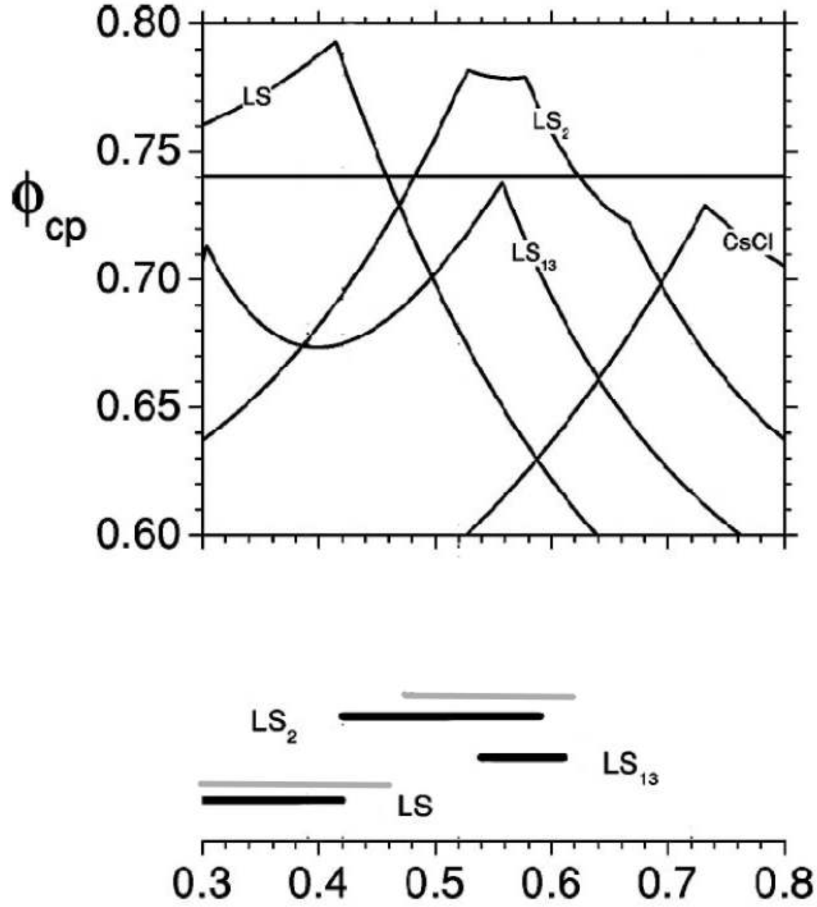

Fig. 2.2. Graph of the size ratio ($\frac{R_S}{R_L}$) versus the packing fraction (ϕ_{cp}) for several stoichiometries of binary hard sphere mixtures[19]. The predicted stability range using packing fraction comparison (grey) and cell theory [6] (black) shown below.

Experimentally, there are additional parameters in addition to the size ratio of the spheres to consider. The volume fraction of each species of sphere mixed into the solution can have a significant effect on the resulting structures. Despite the additional challenges, experimentally all of the stoichiometries shown in figure 2.2 have been made. The AB_13 (LS_13) and the CsCl version of the AB structure have been made, even though they are predicted as marginally stable at best [19].

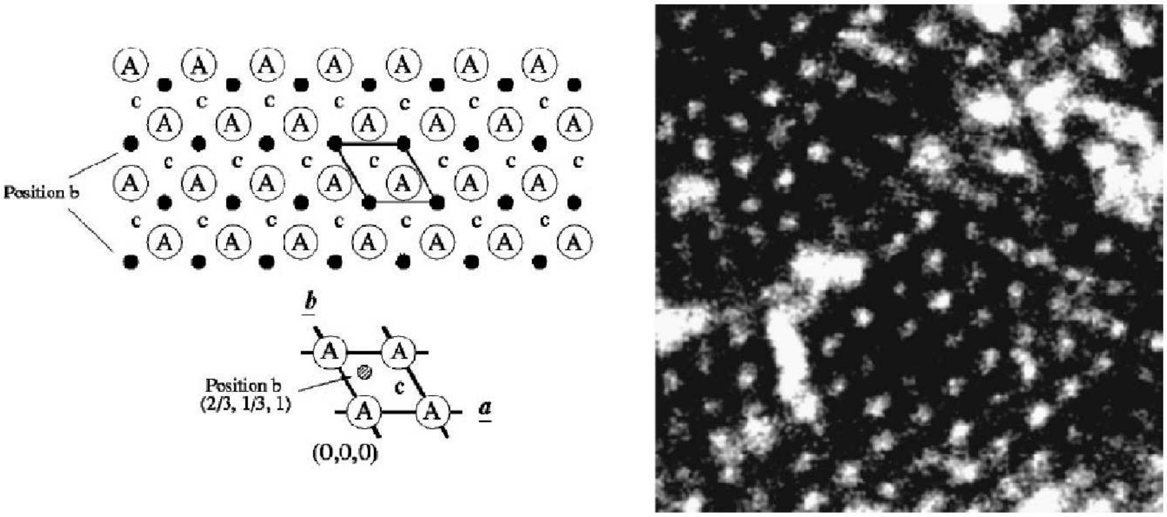

(a)

(b)

Fig. 2.3. a) Shows the (001) face of the NaCl crystal, The positions of the large spheres are labeled **A**, the small spheres occupy the **b**, while the **c** sites are vacant. b) A fluorescense confocal scanning laser microscopy (CSLM) image of the ordered binary crystal formed with the size ratio $\alpha = 0.39$. The hexagonal pattern of the small **b** fluorescent particles is visible [19].

In the smallest size ratio the NaCl crystal is predicted to be preferred over phase separation ($\frac{R_B}{R_A}$=(0.20-0.44) when using the packing fraction as the figure of merit. Hunt, Jardine and Bartlett first created the NaCl structure out of PPMA (methyl methacrylate) particles. Shown in figure 2.3 is a fluroescence confocal scanning laser microscopy (CSLM) image showing the NaCl crystal structure where the smaller spheres are visible in the image [19]. Hunt was unable to crystallize the alternative CsCl structure for AB stoichiometry at a size ratio of $\frac{R_A}{R_B}$=0.72. In 2001, Schofield created a CsCl crystal superlattice from PPMA particles at a size ratio of $\frac{R_A}{R_B}$=0.732. The resulting structure is imaged with a scanning electron microscope and is shown in figure 2.4. This structure is predicted to be unstable by space filling consideration. Schofield found that the CsCl structure disappeared over time, indicating a metastable state at this most optimal size ratio. [49]

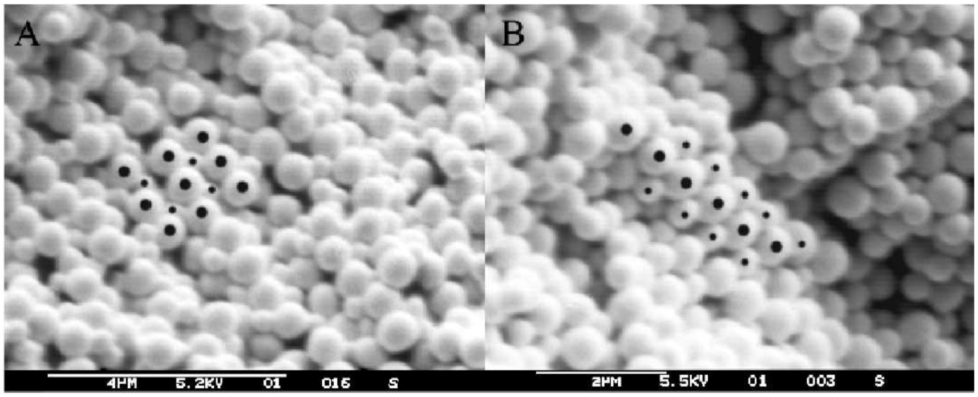

Fig. 2.4. Scanning electron microscope images of particles packed in the CsCl structure. A) Shows a large region of CsCl ordering with square packing of the large spheres, with smaller spheres at their center. B) The central portion shows the square face of cubes made of smaller spheres with the larger spheres in the middle of each.

In addition to the AB stoichiometry, AB_2 and AB_{13} stoichiometries have also been crystallized in the size ratio ($\frac{R_A}{R_B} = 0.58$) out of latex particles [14]. The AB_2 and AB_{13} superlattices are isostructural with AlB_2 and $NaZn_{13}$ and also found naturally in opals [47, 48]. The AB_2 and AB_{13} have also been found made ot of $PbSe$ and Fe_2O_3 nanocrystals with a size ratio 0.55. The AB_2 lattice is a hexagonal layer of smaller spheres with the larger spheres forming a triangular lattices in the center of each hexagon separating the layers. The AB_2 lattice is depicted in figure 2.5 and diffraction patterns are shown from three different angles [45].

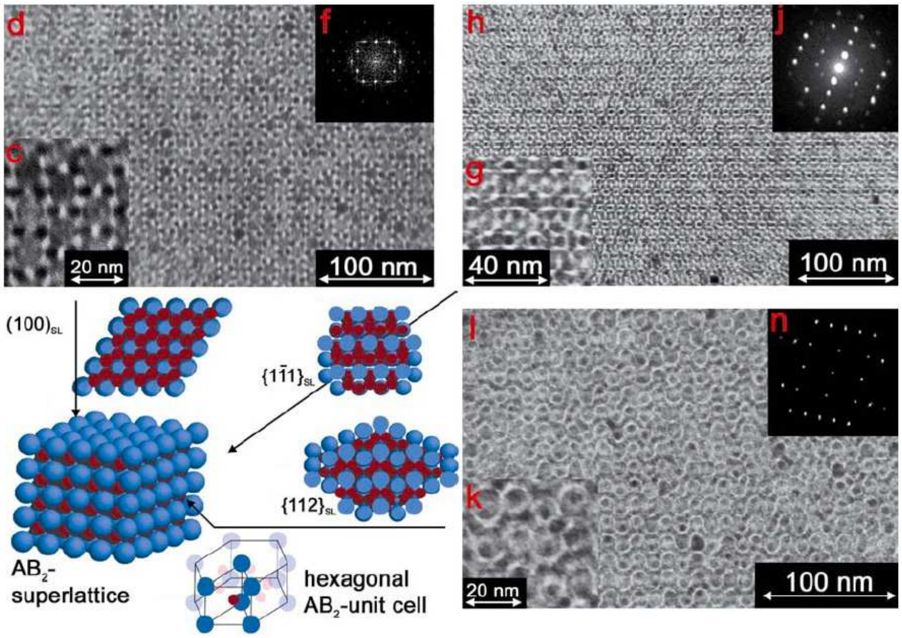

Fig. 2.5. The AB_2 crystal structure constructed from $PbSe$ and Fe_2O_3 nanocrystals. Scanning electron microscope images are shown and their corresponding diffraction pattern from three different angles [45]

The AB_{13} structure has a cubic lattice of larger spheres with a 13 vertex isocahedron filling the center of the cubic space. This structure is very close to the phase separated packing fraction of 0.74 in the size ratio $\frac{R_A}{R_B}$=0.58. The AB_{13} has also been crystallized from $PbSe$ and Fe_2O_3 nanocrystals and the structure along with experimental results are shown in figure 2.6.

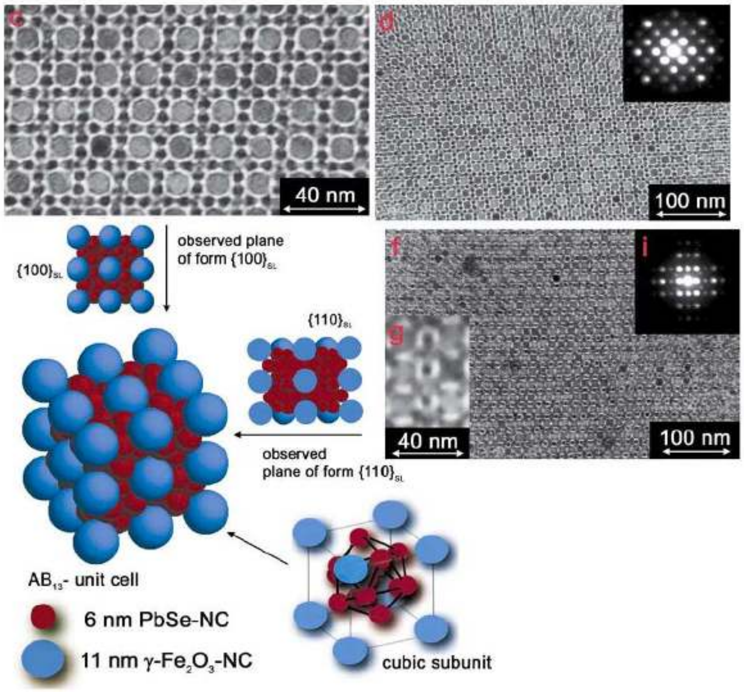

Fig. 2.6. The AB_{13} crystal structure constructed from $PbSe$ and Fe_2O_3 nanocrystals. Scanning electron microscope images are shown and their corresponding diffraction pattern from three different angles [45]

Experimentally all binary nanoparticle superlattices that are predicted to be stable or metastable have been synthesized. One may increase the number of possible structures by increasing the number of different particles in a mixture, functionalizing the particles to have an interaction other than just hard sphere repulsion, by creating new shapes or by creating clusters of composite nanoparticle molecules. Increasing how many types of particles in a mixture becomes complicated very quickly due to the rapid increase in the number of possible configurations. This has limited experimental trials in this area. While, functionalizing particles and creating new shapes or composite particles has been an area with much progress. Certain nanoparticles such as PbSe or Au nanoparticles can be charged positively or negatively by adding surfactant molecules or by exposure to oleic acid. Various mixtures of PbSe, Au, Fe_2O_3, and Pd have been experimentally used in production of a wide variety of nanoparticle superlattices, in addition to the lattices formed by hard spheres. Figure 2.7 shows a vast array of superlattices formed experimentally by Shevchenko et. al. [51]. Chemical isostructures are listed where present. As shown in figure 2.7, by adding the additional freedom of adjusting the charge a much wider variety of crystal structures has been formed.

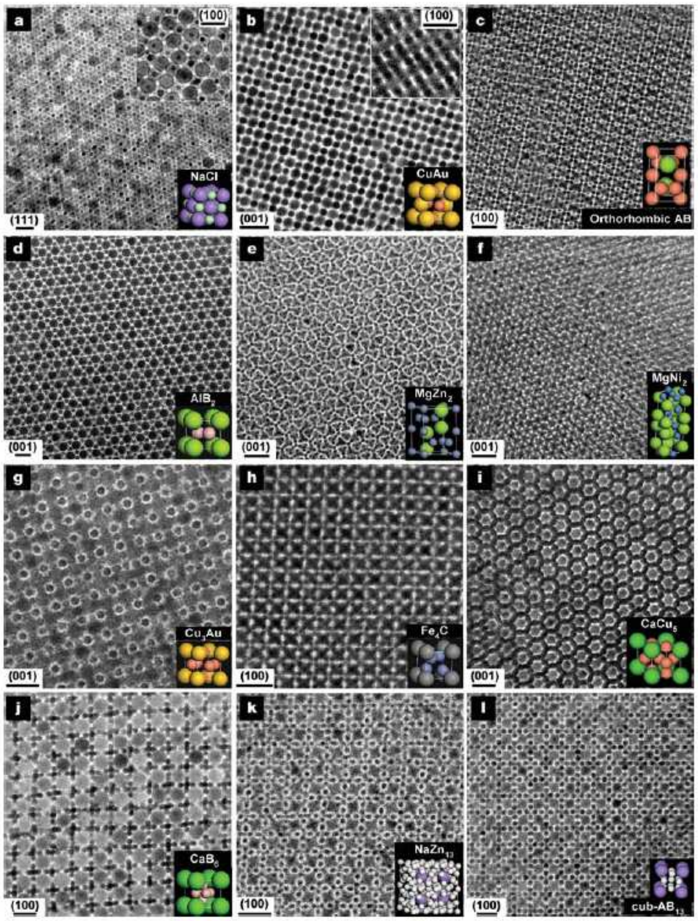

Fig. 2.7. TEM images of a wide array of nanocrystal superlattices formed from mixtures of PbSe, Au,Ag, Fe_2O_3, and Pd. Scale bars represent 20 nm. a) 13.4 nm $\gamma - Fe_2O_3$ and 5.0 nm Au, b) 7.6 nm PbSe and 5.0 nm Au, c) 6.2 nm PbSe and 3.0 nm Pd, d) 6.7 nm PbSe and 3.0 nm Pd, e) 6.2 nm PbSe and 3.0 nm Pd, f) 5.8 nm PbSe and 3.0 nm Pd, g) 7.2 nm PbSe and 4.2 nm Ag, h) 6.2 nm PbSe and 3.0 nm Pd, i) 7.2 nm PbSe and 5.0 nm Au, j) 5.8 nm PbSe and 3.0 nm Pd, k) 7.2 nm PbSe and 4.2 nm Ag, and l) 6.2 nm PbSe and 3.0 nm Pd [51]

Many other different types of nanoparticles have been created. Particles that have various shapes or clusters of particles, such as ellipsoids, bumpy spheres, triangular particles,spherical particles with internal structure, and spherical particle composites [68, 67, 51, 56, 11]. Depicted in figure 2.8

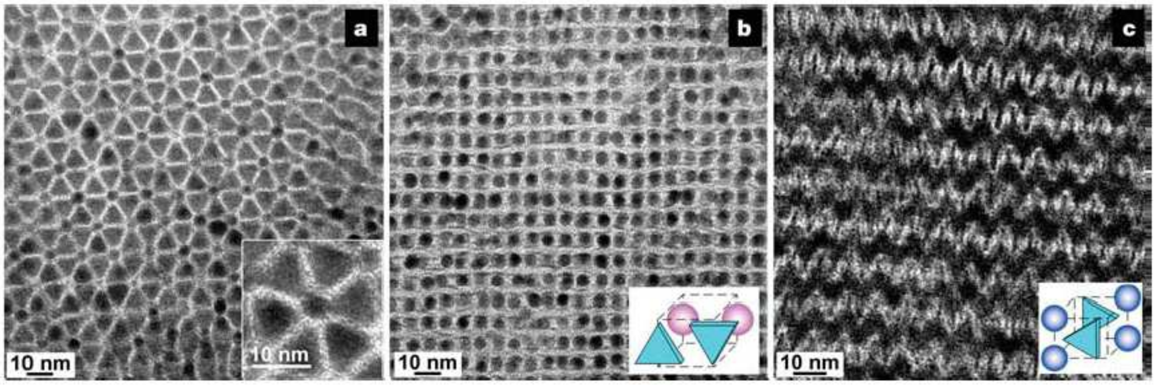

Fig. 2.8. a) and b) Self-assembled from LaF_3 triangular nanoplates (9.0 nm side) and 5.0 nm Au nanoparticles) c) Self-assembled from LaF_3 nanoplates [51].

As you can see from 2.8, adding some non-isotropic structure to a particle can add a variety of different superlattices, even in a two component mixture. Beyond simple geometric shapes and spherical composite particles, interesting structures may be possible from more complicated particles such as those shown in figure 2.9.

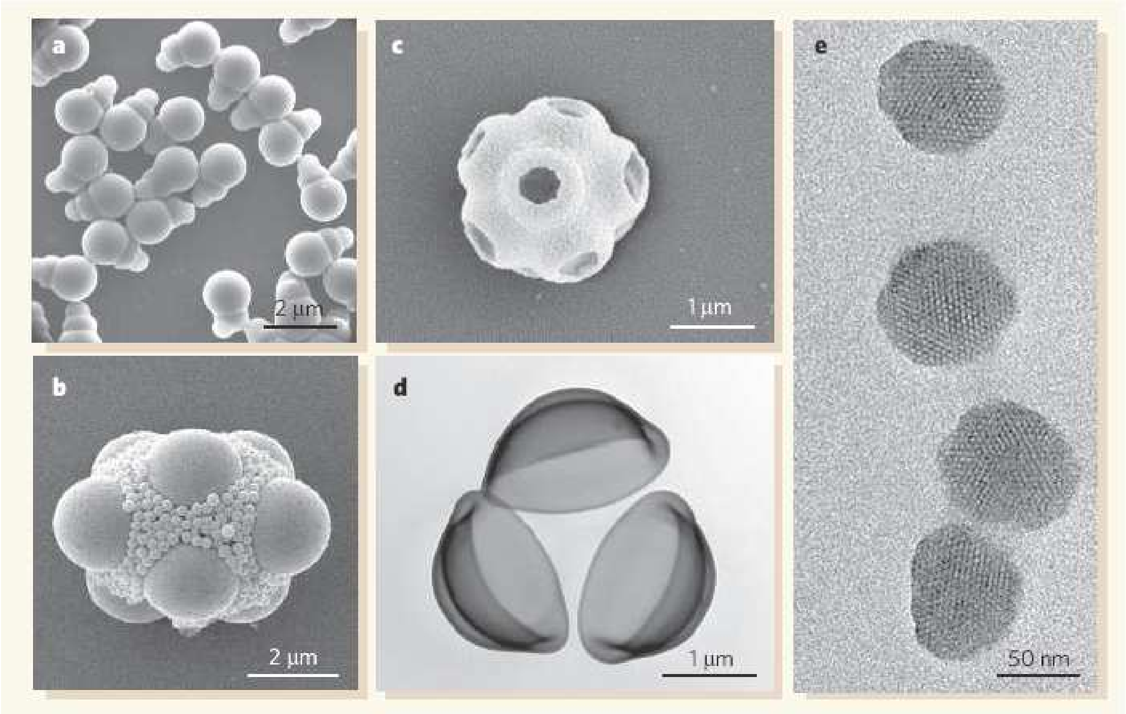

Fig. 2.9. a) “Ice-cream cones” resulting from repeated polymerization and phase separation of different compositions, b) and c)Created with controlled drying in a water-in-oil emulsion, d) Created trhough silica-deposition on liquid crystal phases, e) Formed through osmotic stress deformation of hybrid siloxane shells after growing them on monodisperse oil droplets [56]

Such a wide variety of possible structures is in need of a method to reduce the vast phase space of possibilities to regimes in which interesting results are more likely to occur. In the following section we describe a method for searching through the phase space to find areas of interest for future experiments to explore.

2.4 Method

As discussed earlier in this chapter genetic algorithms have already been applied to finite systems such as clusters (C_{60} and Si_n) and point charges on shells [7, 16, 34]. These bounded structures were parameterized with simple lists of atomic coordinates and then bisected in real space and merged to form progeny. This real-space bisection works well for clusters, since the importance of short-range interactions implies that contiguous sub-sets of atoms (or point charges) from each parent will tend to define valleys in the fitness landscape. These subsets can be merged sensibly to make progeny, with the new interactions occurring mainly at the interface of the two portions from each parent.

An extended system such as a crystal cannot be effectively bisected in this way, since the lattice vectors do not define local bond angle or bond length information. It is unclear how to recombine portions of an infinite system in a sensible way to retain some of the local character of the original structures. Instead, we must find an alternative parameterization of the lattice periodicity, one which propagates local structural information to the next generation. To this end, we represent the crystal as a multi-headed "hydra" H of displacement vectors: $H \equiv (\vec{B}_1, \vec{D}_1, \vec{B}_2, \vec{D}_2, \vec{B}_3, \vec{D}_3, \vec{B}_4, \vec{B}_5, ...\vec{B}_N)$. The vectors $\{B\}$ interconnect nearby particles within a single unit cell and the vectors $\{D\}$ connect particles in adjacent unit cells and thereby define the periodicity. N is the number of particles in the unit cell. In d dimensional space, the hydra has a total of $Nd + d^2$ elements; (we take $d = 3$). The projections to neighboring unit cells are spread throughout the hydra and always interconnect distinct particles; this allows maximum flexibility in representation while maintaining predominately nearest-neighbor displacements. Since the projections $\{D\}$ to neighboring cells can represent nearest-neighbor interactions (unlike standard lattice vectors), bisecting the hydra and recombining disparate halves tends to preserve the local motifs of proximal inter-particle separations and angles; these motifs are the primary determinants of valleys in the fitness surface [62]. We are able to retain some of the local structural characteristics, with the possiblity of having large overall changes to the structure via propogation of the displacement vectors ($\vec{D}$). An example showing how two structures that look very different could yeild a structure with a nearly square lattice is given in figure (2.11). In the example (Figure 2.11) each parent contains some local bonding, when combined in the appropriate way leads to a child with a nearly square lattice.

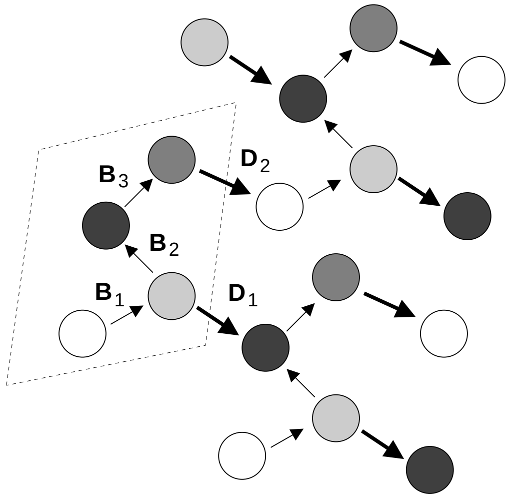

Fig. 2.10. The “hydra” representation of a crystal uses a chain of linked displacement vectors within and between unit cells to enable an efficient exploration of the energy surface. Only two dimensions are shown for clarity. The term “hydra” refers to a body B with D heads extending outwards. The gene sequence is e.g. $(\vec{B}_1, \vec{D}_1, \vec{B}_2, \vec{D}_2, \vec{B}_3)$.

We create a random initial population of structures by concatenating a set of interparticle displacements with random directions and an average length centered about a typical nearest-neighbor separation. This includes the projections $\{D\}$ to adjacent unit cells, so that they also define nearest-neighbor bonds. The angle between portions from each parent is an arbitrary angle depending on the absolute orientation of each parent. This angle is first optimized with a conjugent gradient local optimization keeping the relative positions of the portion from each parent fixed. Following the relaxation of the arbitrary joint angle, any highly unfavorable structures are immediately rejected, provided they do not fall within a predefined minimum fitness threshold. Generally, the threshold was set so that structures with a positive binding energy were rejected before local relaxation. This criterion is fairly restrictive since it is very easy to generate coordinates with overlapping particles. However, the structure generation is very fast allowing us to overcome this restriction. The overall algorithm is most efficient when the input structures to the local relaxation are sufficiently stable that structural motifs are reasonably well preserved during the local relaxation. Two parents are chosen at random from this population and mated into a child structure by selecting the first p vectors from hydra H^i and the remaining vectors from H^j and varying the crossover point p randomly from one mating to another. For example: $H^{\mathrm{child}} = H^{\mathrm{i}} \star H^{\mathrm{j}} = (\vec{B}^{\mathrm{i}}_1, \vec{D}^{\mathrm{i}}_1, \vec{B}^{\mathrm{i}}_2, \vec{D}^{\mathrm{j}}_2, \vec{B}^{\mathrm{j}}_3, \vec{D}^{\mathrm{j}}_3, \vec{B}^{\mathrm{j}}_4)$ with a crossover after the third vector. Structural diversity must be maintained from generation to generation to prevent the population from self-trapping as a set of clones within single local minima (i.e. genetic drift). We evaluate:

$$\hat{H}^i \cdot \hat{H}^j, \tag{2.1}$$

a dot product between two structures (where $\hat{H} = \vec{H}/|\vec{H}|$ is a hydra normalized to an overall length of one).

We then accept a child into the population only if:

- its maximum normalized dot product against the existing population does not exceed a fixed amount (~ 0.8) and,
- its absolute fitness difference from all extant structures exceeds a fixed amount ($\sim$ 0.5% of the typical energy scale for relaxed structures).

To broaden the search space, 10 to 20% of bonds suffer a small random fluctuation (mutation) of 5 to 10% (Gaussian standard deviation) in the inter-particle separation before the complimentary halves are recombined. Since the joint between the pieces from each parent is arbitrary, we first optimize just the angular orientation of this joint (using the potential function defined below), moving the two respective halves as rigid units. Each child is then fully relaxed to the local energy minimum. Children are generated in batches of 10 to 20 and are inserted into the breeding population if their figures of merit are within those of the top 20 current active structures and the similarity threshold defined above is satisfied. The generations proceed, retaining the top 20 structures at each iteration, until a preset number of satisfactory progeny has been generated (typically 100–200 generations).

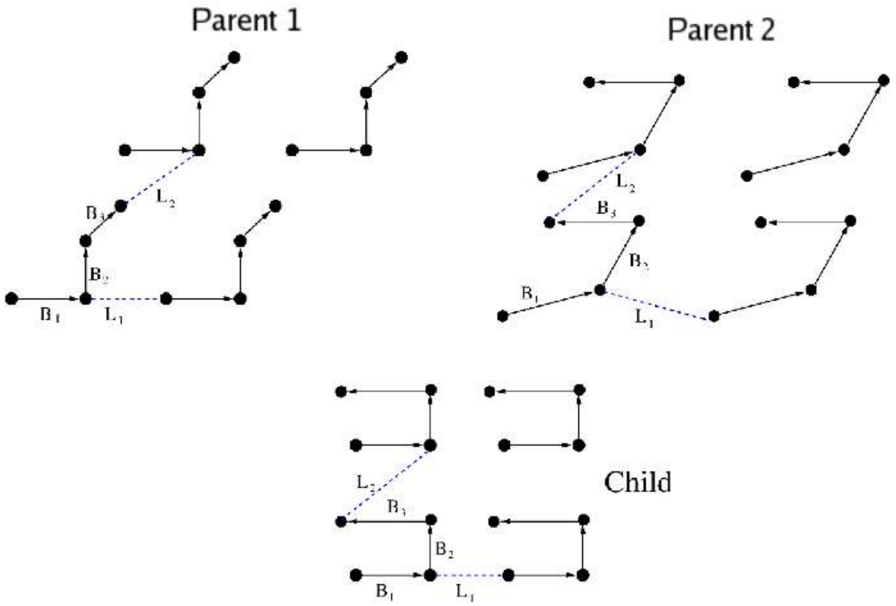

Fig. 2.11. Hydra Mating Illustration: The gene sequence is $(\vec{B}_1, \vec{L}_1, \vec{B}_2, \vec{B}_3, \vec{L}_2)$, where the first portion $(\vec{B}_1, \vec{L}_1, \vec{B}_2)$ is kept from parent 1 (upper left) and the latter portion $(\vec{B}_3, \vec{L}_2)$ is kept from parent 2 (upper right) to create a child that has a closer packed nearly square lattice (bottom).

We apply this algorithm first to crystals formed from hard spherical nanoparticles, since they provide an easily evaluated approximate fitness function. Rather than directly modelling the entropic contributions from interacting hard-core particles, we instead target the packing density as the ultimate figure of merit (as discussed earlier) and use the binding energy from a fictitious two-body hard-core potential (with a long-range attraction) as a surrogate fitness function to generate densely packed structures. The potential :

$$V = \epsilon \left[(\frac{\sigma}{r})^m - (\frac{\sigma}{r})^n \right] \tag{2.2}$$

,with $m = 48$ and $n = 24$ ensures a well-defined sphere radius. The particular m and n chosen has little effect on the final results, so long as the potential has a generic weak longer-ranged attraction and a core hard enough to allow a precise definition of the packing fraction. Although we select on this fictitious binding energy, the final optimized solutions are evaluated based on their packing fraction; we find good agreement with prior results for known crystalline packings. We have reproduced the packing fraction and size regimes in which they are preferred as shown in 2.2 in addition to finding close packed spheres with a packing fraction of 0.74 for supercells up to ten spheres per unit cell. As demonstrated in the seminal early work of Hachisu and Yoshimura [15], the packing fraction of hard-sphere colloids is a good first approximation for the relative stability of competing colloidal phases, particularly if surface charging effects are relatively weak or highly screened. Of course, packing fraction as a figure of merit does not contain the more subtle higher-order entropic effects that can distinguish structures of identical packing fraction, such as fcc and hcp.[6]. This figure of merit is also highly computationally efficient, so it is very useful for an initial application of the method [6].

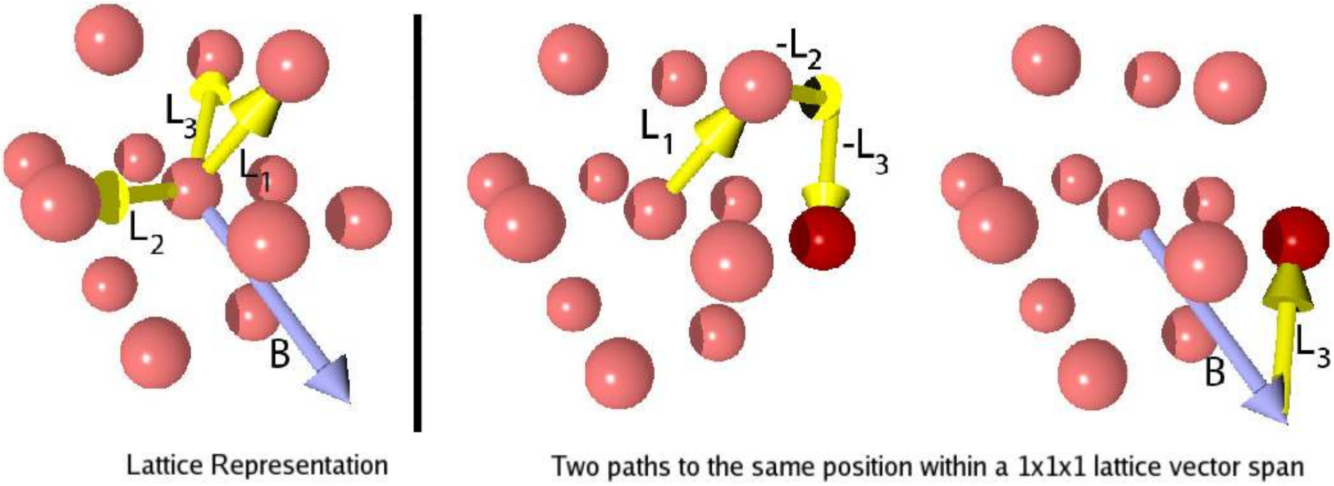

Fig. 2.12. Figure illustrating the overlapping particle problem: Two different combinations of lattice and basis vectors give nearly identical particle coordinates. This can occur when basis vector(s) are longer than lattice vectors and all pair interactions are not calculated. The lattice vectors and basis vectors are listed in table 2.1 along with the other overlapping particle combinations within the span calculated Basis and lattice vectors found for close packed spheres (left), Two paths to an overlapping particle (right).

Since every unit cell is identical, the most computationally efficient way to evaluate the potential would seem to be as a sum of pair contributions outward from a central unit cell, to some cutoff distance. It would be natural to try to construct the set of atoms that lie within this cutoff by finding the atoms that are associated with every unit cell in some large $M \times M \times M$ box of unit cells that surround the central cell,

L_1	L_2	L_3	B
(-0.48,0.86,-0.32)	(0.22,0.47,0.90)	(0.30,0.45,-0.90)	(-1.29,-0.50,0.58)
Particle 1	Particle 2	Position	
$L_1 - L_2 - L_3$	B+L_3	~(-0.99,-0.06,-0.31)	
$L_2 + L_3 + B$	$L_1 - L_3$	~(-0.77,-0.41,0.57)	
$-L_1 + L_2 + L_3 + B$	$-L_3$	~(-0.30,-0.45,0.90)	
$-L_1 + L_3 + B$	$-L_2 - L_3$	~(-0.51,-0.92,0.01)	

Table 2.1. Lattice vectors and basis vectors for an example pathologic structure which results in overlapping particles within the 1x1x1 lattice vector span. Four particles have overlapping particles in this example whose interaction is not calculated in a typical energy calculation evaluated from a central unit cell outward.

and then retaining all such atoms that fall within the cutoff distance. If M is large enough, one would expect this construction to find each and every atom that is in or close to the central unit cell. However, if this method is actually used to evaluate the potential, then the highly efficient genetic search can find nonphysical structures for which this construction does *not* generate every relevant atom, yet these (pathological) structures evaluate to an energy more favorable than that of any physical structure. These pathological structures stretch one or more of the B basis vectors to a length comparable to the cutoff distance itself. Atoms described by such long basis vectors can "leak out" of the $M \times M \times M$ box, so that the unit cells near the center of the box are not identically populated. Specifically, these long basis vectors arrange themselves such that two atoms are placed directly on top of each other, but the $M \times M \times M$ construction does not find both such atoms for the central unit cell itself; it finds them only for the neighboring cells. This then generates a spurious nearest-neighbor coordination number (greater than twelve) for atoms in the central cell, which corrupts the energy calculation when the pair potential is evaluated outwards to the surrounding atoms. Specifically, the central cell is “missing” one particle, and that particle, which is present in one or more neighboring cells provides the extra neighbors leading to the problematic coordination numbers. An example of this situation is shown in figure 2.12 with the resulting lattice vectors and combinations that give overlapping particles within the $M \times M \times M$ box is given in table 2.1. Extending the span M of the lattice vectors doesn't help, since the basis vectors simply stretch further. We eliminate this pathology by calculating the energy of interaction between *all* atom pairs within the $M \times M \times M$ box. This more thorough sampling prevents the algorithm from avoiding the energetic penalty of placing atoms on top of each other, so it suppresses the nonphysical structures. This pathology, which is avoided by summing interactions over all pairs within an entire block of unit cells, is actually a testament to the thoroughness of the genetic search.

2.5 Results

As a test, we first search for the known dense-packed unary and binary structures A, AB and AB_2 formed from spherical constituents[47, 48, 44, 1, 19]. In all cases, including artificial supercells up to 10 formula units, the genetic search finds the correct solution. (For our all of our calculations, including the binary and ternary calculations to be described below, a similar potential was used, with a constant well depth and an equilibrium pair separation equal to the sum of the radii of the two relevant spheres). A competing random search, which uses the same initial structure generation and local optimization as the genetic search, ranges from 3 to 100 times slower, with the slowest performance in the larger cells. For five sphere super cells and larger the random search failed to find the optimal structure. For supercell binary systems the random search

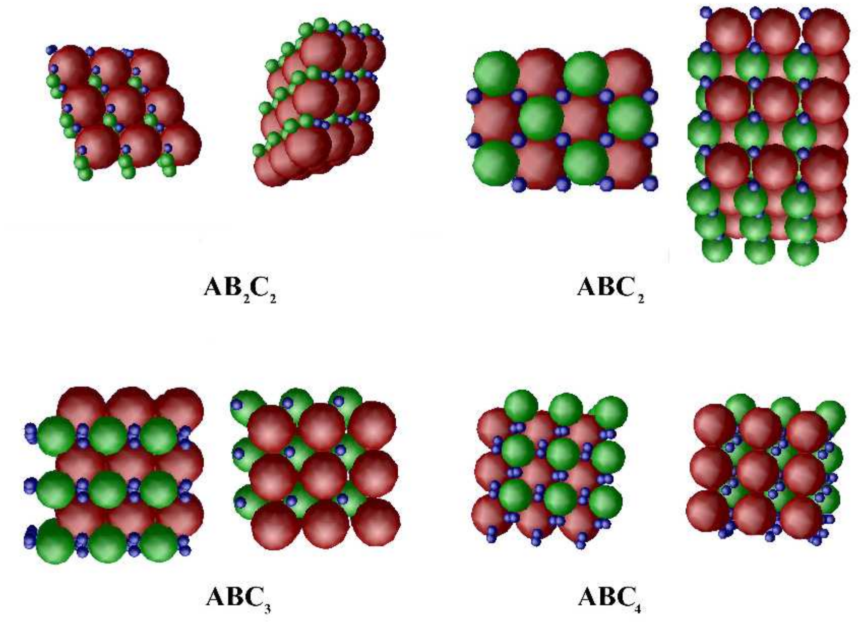

AB_2C_2 ABC_2

ABC_3 ABC_4

Fig. 2.13. Preferred self-assembled ternary structures (two views of each).The AB_2C_2 structure shows a lattice of large spheres that are nearly close packed with the smaller spheres filling in the gaps. The ABC_x family of structures shows the same underlying structure for A and B spheres with different arrangements of C spheres depending on the stoichiometry.

failed in all runs. The genetic algorithm is superior, particularly for the more richly structured systems, since it can retain and exploit preferred structural motifs.

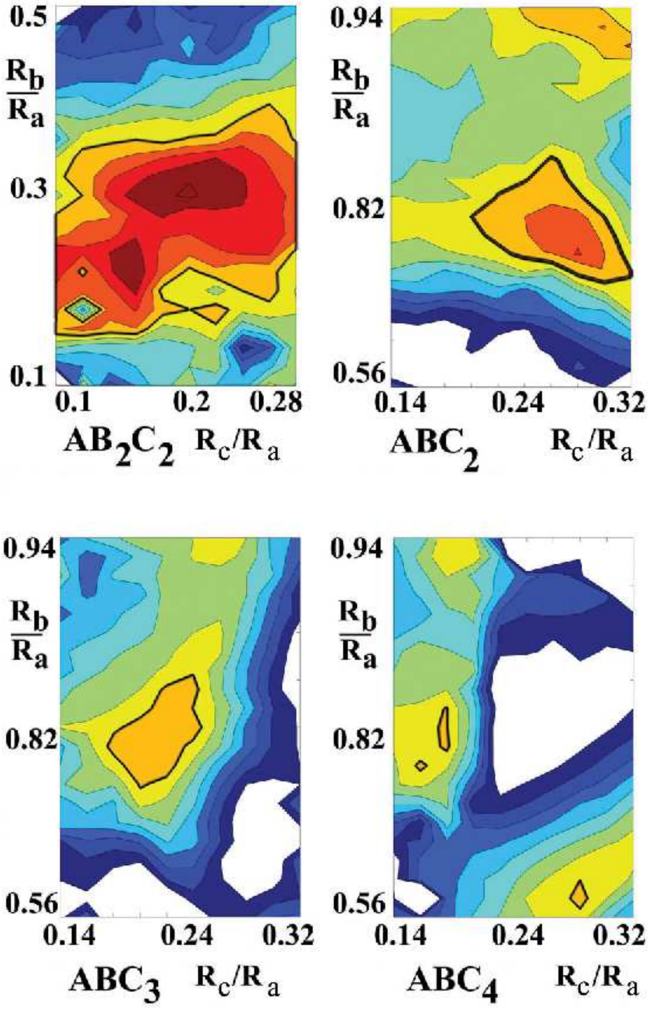

Fig. 2.14. Packing densities of ternary crystals of spherical nanoparticles. The region within the thick lines has higher packing efficiency than phase separated competitors. The continuity of the high packing regions suggests that we have likely found a global maximum packing fraction. The large region with packing fraction above 0.74 for the AB_2C2 structure is due to the close proximity of the largest spheres to close packing.

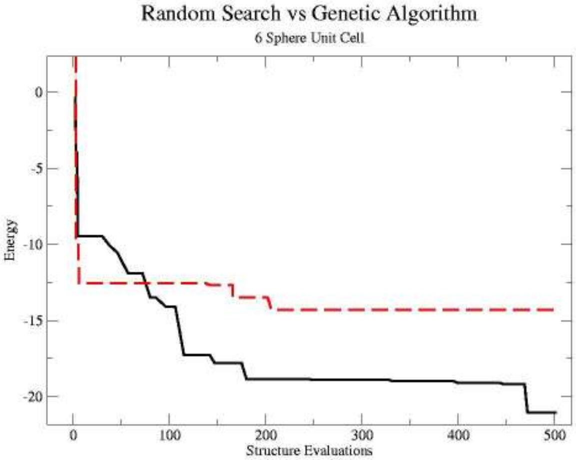

Fig. 2.15. Comparison of the performance of the genetic algorithm (solid black) versus a random search (dotted red). The random search fails to find the close packed sphere optimal case.

We next search in previously unexplored systems such as ternary sphere compounds and fused sphere pairs; (fusion of sphere pairs frustrates phase separation and could force the formation of novel structures). Specifically, we study ABC, ABC_2, AB_2C_2, ABC_3, ABC_4, and fused AB systems, covering the range of relative R_B/R_A and R_C/R_A size ratios from 0.2 to 0.9. Following e.g. Hachisu and Yoshimura [15], the candidate structures' packing fractions were compared to the maximal packing fraction possible among the appropriate ratios of known unary and binary sphere crystals (e.g. FCC ≈ 0.74, NaCl (AB) ≈ 0.793, CsCl (AB) ≈ 0.73, AlB_2 (AB_2) ≈ 0.78) in the applicable size regimes for each structure.

In all cases except ABC we find new structures that are higher in packing density than the competing phase-separated systems. Due to computational constraints, for the ternary systems we study a single formula unit per unit cell. The smooth contour surrounding the high packing efficiency region in Figure 2.14 suggests that we have likely found a global maximum packing fraction at this stoichiometry. Since structures of higher packing efficiency could exist with more formula units per cell, the results here provide a lower bound on the range of $(R_B/R_A,\ R_C/R_A)$ phase space in which novel crystals could be found.

The $ABC_{2/3/4}$ stoichiometries form a closely related family of layered tetragonal or orthorhombic structures. In the archetypal ABC_2, the largest (A) spheres contact each other in a two-dimensional square lattice; the medium (B) sphere then fill the depressions within this layer while the smallest (C) spheres fill the gaps between the B spheres; (see Fig. 2.13). For ABC_2 the B–C layers have the structure of a Cu-O perovskite plane and attain a highest packing fraction of 0.78 when $R_a = 1.0$, $R_b = 0.72$ and $R_b = 0.28$. For comparison, the close-packed packing fraction is 0.74. These optimal sizes yield a simple commensurability: $R_a = R_b + R_c$ and the A-sub-lattice body diagonal of $\sqrt{3}$ leaves holes of $\sqrt{3} - 1 \approx 0.73$ to be filled by B spheres. ABC_3 and ABC_4 differ from ABC_2 in having different arrangements of the C spheres (see Fig. 2.14). The familial similarities suggest that the overall A-B framework is rather robust and that a real system may contain a multi-phase mixture of C placements. Alternatively the C particles may occupy the location of the perovskite apical oxygens in the ABC_3 or ABC_4 structures, in which case size ratios close to the optimal ABC_2 values, $(R_A, R_B, R_C) = (1.0, 0.72, 0.28)$, may be preferred [60]. Similar to the known binary colloidal structures, these ternary systems tend to build around certain special commensurations between the constituents.

In contrast, AB_2C_2 forms distorted triangular-packed layers of large spheres with the medium and small spheres filling in the gaps. This structure attains an optimal packing fraction of 0.77 at $R_b/R_a = .24$ and $R_c/R_a = 0.16$. The proximity of the A sub-lattice to close packing explains the wide range over which this structure has a high packing efficiency (see Fig. 2.14). Both families of ternary structures exhibit layering, which may facilitate applications that require the isolation of distinct subunits, such as self-assembled circuits or waveguides [46, 58]. The contour plots are very smooth. Although each point on this surface results from an independent genetic search, the packing densities of the resulting optimal structures form a smooth manifold. We begin with random initial coordinates and have an unbiased search methods. An unbiased treatment would be unlikely to find many local minima that form a smooth contour as we see in figure 2.14. Since it is unlikely that the search would always find the same smooth continuous family of (non-global) local minima, the smoothness of the contours provides strong heuristic evidence that the algorithm is finding the global optimum.

The ABC_2 system shows a second structure with packing efficiency very close to that of close-packed unary spheres. The smallest (C) spheres form pairs that fill in one interstitial of the larger A-B lattice. This structure is in the same size range as the more optimal packing ABC2 structure (.78). Since the smallest spheres (C) remain together, the possiblity of fusing colloidal spheres together could aid experimental production of these structures since the spheres would no longer be able to separate. Similarly for the robust structure of the A and B spheres in the AB_X family of structures, we may aid crystallization by fusing the larger and medium spheres together (A and B spheres) to prevent phase separation and to help stabilize the crystallization of structures with A-B contacts. This idea of fusing different spheres together as a way to bias the crystallization towards the desired structure can be extended as a way to access new structures.

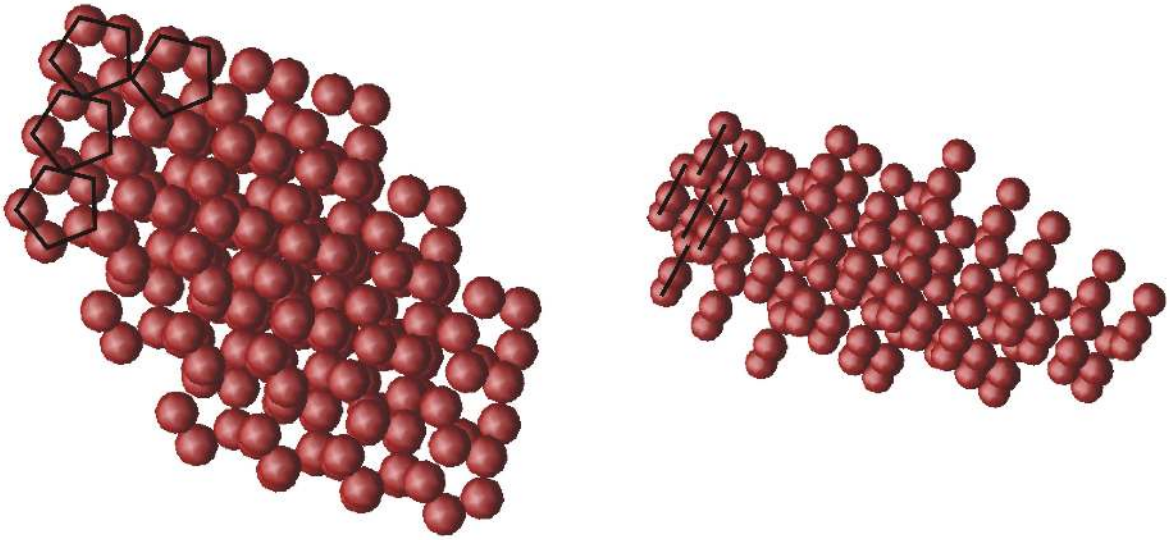

Fig. 2.16. Two views of optimal pentagon “molecule” packing with a one pentagon per unit cell stoichiometry. The pentagons pack in a structure with the pentagons partially overlapping the layer below in a staggered manner.

The fusion of spheres into nanoparticle “molecules” frustrates phase separation by forcing an arrangement of particles that is not efficiently packed to remain. The inability of the spheres to phase separate will force the colloids to find other structures that may normally not form and aid in avoiding closely competing structures. This mechanism may provide a means to access novel structures. We examined several molecular geometries consisting of “molecules” constructed from a single type (size) of sphere. A dimer,

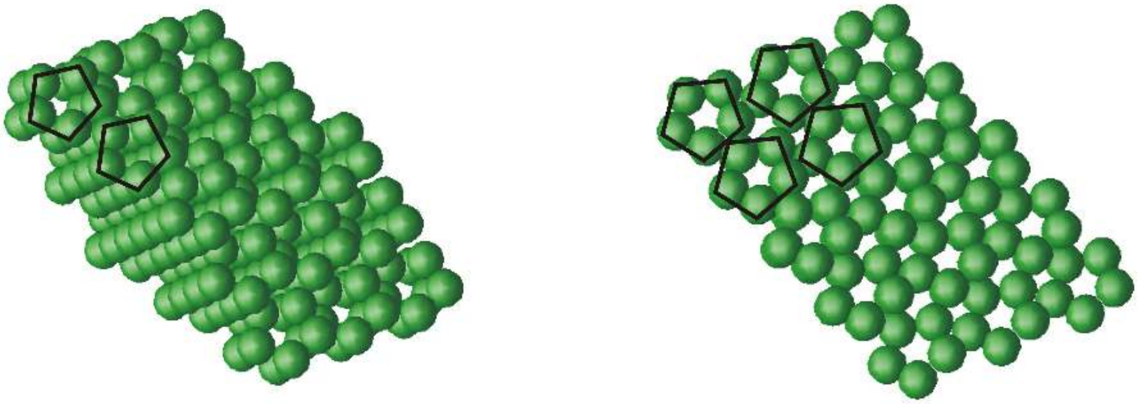

Fig. 2.17. Two views of optimal pentagon “molecule” packing with two pentagons per unit cell. The two pentagon structure stacks the pentagons in columns that are offset to allow the corner of one pentagon to fall into the indentation between layers.

triangular geometry, tetrahedral geometry and pentagonal geometry were all examined. All of the molecule types with the exception of the pentagons are compatible with close packed spheres. Pentagons are incompatible with close packed sphere because any plane of spheres chosen does not contain a pentagonal subunit. The dimer and triangular geometry are clearly contained within one of these planes. For the tetrahedron two planes must be considered since the tetrahedron is a non-planar structure. We found close packing for the dimer, triangle, and the tetrahedron. The dimer and triangular geometry were examined up to four molecules per unit cell and resulted in close packed spheres. The tetrahedral geometry can only form a close packed arrangement when grouped in pairs. One tetrahedron is flipped upside down and placed adjacent to the other tetrahedron forming two layers of four spheres. This arrangement is compatible with close packed spheres. We find close packed spheres from the genetic algorithm output with two tetrahedra per unit cell. Although regular tetrahedra are unable to completely tile 3-d space, we can fill the optimal sphere packing arrangement with tetrahedrally arranged spheres. This is due to the indentation available in the center of each face of the tetrahedra. Pentagonal molecules constructed from unary spheres were examined up to a two molecule per unit cell configuration. The resulting structures found are shown in figure 2.16 and figure 2.17. Using two pentagons per unit cell the best arrangement found is to stack the pentagons directly on top of each other and stagger these columns allowing one of the spheres in the pentagon to fill in the indentation available between layers in the adjacent column. Examining figure 2.17 you can see that in the center of the four outlined columns of pentagons there is a sphere that is unable to find an indentation to pack more efficiently. This inefficiency is due to the incompatibility of the five-fold pentagonal geometry with filling space. This space filling frustration makes the pentagonal molecule system an interesting system to examine. One interesting property of the two pentagon structure shown in figure 2.17 is that the pentagons are stacked directly on top of each other. This is surprizing since this leave a large void in the colum of pentagons. Due to this frustration, a system of pentagonal molecules may form a much larger unit cell than we can examine due to computational constraints.

Fusion of spheres spheres of different sizes into molecules creates an additional degree of freedom that allow new structures to become preferred. The fusion of spheres into nanoparticle “molecules” frustrates phase separation and provides an interesting mechanism to induce novel structures. AB stoichiometry spheres show several well-known phases: around $R_b/R_a \sim 0.22$, 0.41, and 0.73 the system prefers the ZnS, NaCl/NiAs, and CsCl structures respectively. The range from 0.50 – 0.65 has poor packing efficiency and therefore hold greatest promise for novel structural accomodations if phase separation is frustrated by fusion. In this range, we find a new self-assembled $(AB)_2$ structure wherein the larger spheres form a staggered but impenetrable layer, with the smaller spheres tilting cross-wise into paired zig-zag wires that run in well-separated parallel rows. This interesting structure is preferred over a wide range of R_b/R_a (0.5 – 0.65), assuming a unit cell containing two dimer pairs. These self-assembled zig-zag rows could either form nanowires themselves (if the small spheres are metallic) or provide a template for the arrangement of additional nanorods onto the crystal's surface. A competing structure (but with a slightly smaller packing fraction) in which the smaller spheres are separated is also observed. The nanowire structure could be further favored by adding a small attractive contact interaction between the smaller spheres.

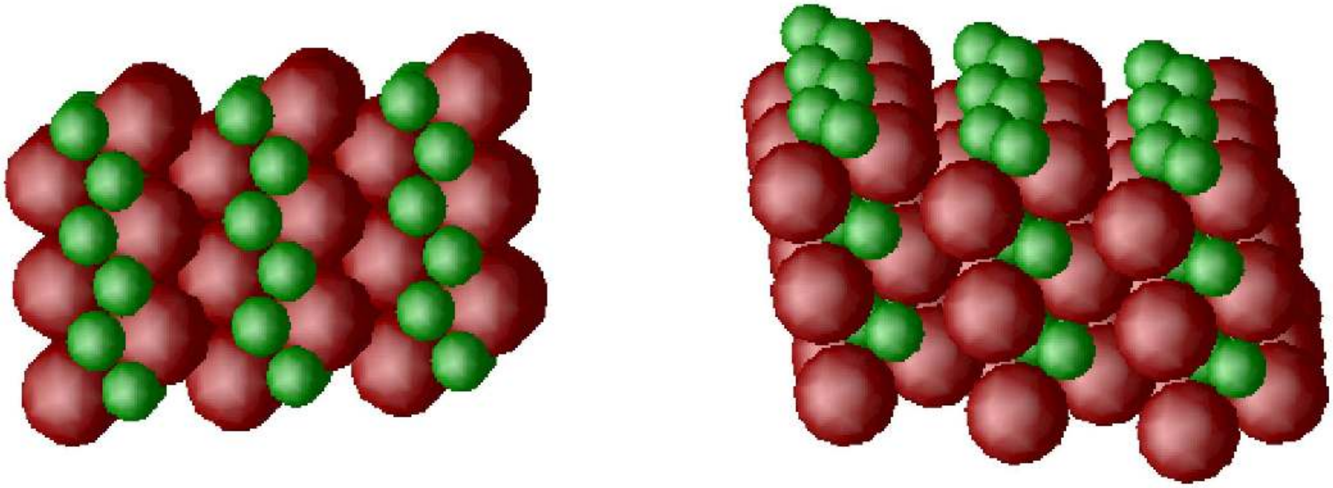

Fig. 2.18. Preferred structure for a fused-sphere system. The smaller spheres align to form self-assembled zig-zag nano-wires ($R_b/R_a = .58$) (two views). The packing efficiency is .757 in this two dimer unit cell $(AB)_2$.

Once these target dense-packed structures are known, one could further encourage their formation by chemical functionalization of the particle surfaces to produce explicit nearest-neighbor interactions that reinforce the preferred contacts. Particles with functionalized surfaces can yeild a richer set of possible structures such as patchy colloidal particles in a diamond lattice [70]. The algorithm is straightforward to parallelize and therefore could be extended to handle more computationally intensive figures of merit[2, 3] such as self-consistent density functional total energy calculations for atomic-scale crystals or screened electrostatic effects in colloidal crystals with strong surface charge. Some ionic colloidal crystals have been realized experimentally by Leunissen et. al. [33]. In addition to the more complicated building blocks constructed of multiple spheres and elliptical shapes, spheres with very intricate internal structures have been constructed [11]. Using polymers with different types of interactions, the colloidal spheres could have very complex interactions. These interactions could be taylored to prefer some of the structures presented here or some new crystals. As we have seen with the fused-sphere dimer system examined, restricting the available configurations to the particles can lead to very interesting structures. The ability to predict promising parameter regimes for the self assembly of extended periodic systems should aid in the search for new materials with interesting electrical, optical or chemical properties. We have demonstrated a technique that can be extended to provide guidance for future experiments reducing the vast search space to target regimes that are most likely to yeild new materials.

Chapter 3

New Forms of Silicon

3.1 Triple Bonded Silicon Crystal Lattice

3.1.1 Overview

The importance of silicon is very clear in today's world. Silicon is the basis for the information technology industry. Silicon is the basis for computer chips and most of the semiconductor industry. Silicon is present in nearly all of the electronic devices in homes throughout the world. Silicon also has a wide variety of applications beyond technology. Silicon-based products are also used in various types of protective coatings and sealants used in industrial applications. The health care field uses silicon based materials to provide lubrication for syringes and tubing for dialysis. Silicone based products are also used in many household cleaners in addition to providing a waterproof coating for fabrics.The variety of applications and the importance of each of them shows how important silicon based materials and technology are to our society. Understanding silicon bonding, structures and new possibilites that may be plausible is therefore a very important subject for the possible development of new products.

Double and triple bonds are common in carbon chemistry, but are unusual for silicon and the heavier elements due to the weak π bonding between these atoms [54, 12, 50]. Stabilizing the Si-Si triple bond has been a subject of recent interest in trying to expand the availability of novel silicon structures [25]. Recently a molecule containing a Si-Si triple bond was synthesized experimentally. This molecule was stabilized using bulky protective chemical groups to prevent the very reactive silicon triple bond from breaking[50, 61]. In synthesizing the molecule, a chain of silicon, with bromine filling all open bonds is used (Shown in figure 3.1). The bromine atoms are removed in the reaction, leaving the bulky groups on each end of the chain as a protective barrier for the newly formed silicon triple bond.

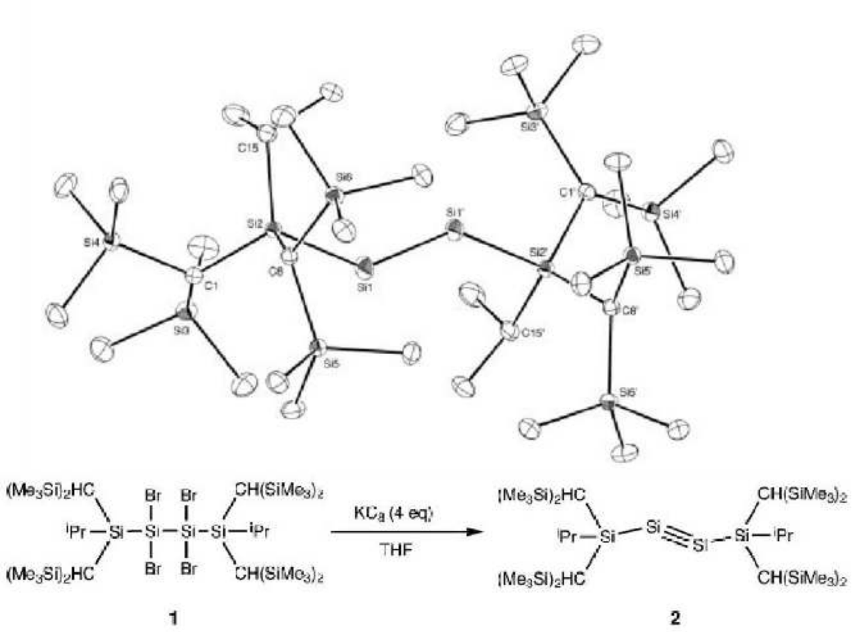

Fig. 3.1. An illustration of the reaction process in creation of the silicon triple bond in a molecule [50] and the resulting molecule.

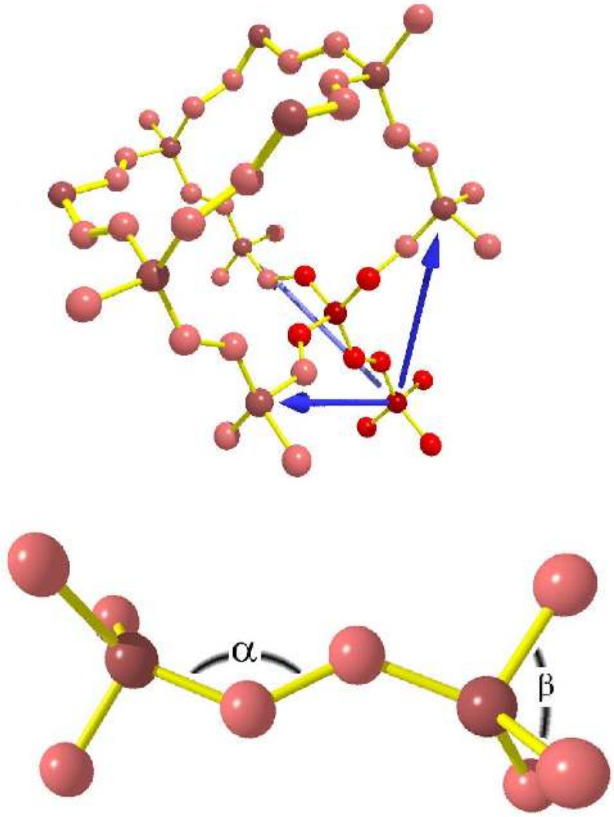

Fig. 3.2. Core region of molecule (bottom) constructed by Sekiguchi ($\alpha = 137.4^\circ$, $\beta = (106.4^\circ - 114.7^\circ)$)[50]. We use this core region as our basic unit to constructing dilated diamond crystal lattice (top). Atoms that have four sp3 bonds are shaded darker than the triple bonded atoms.

3.1.2 Structure

Our prime motivation is to investigate Si=Si multiple bonds in the solid state. We would like to understand the properties of such solids in order to gain insight into the bonding character of silicon multiple bonds as a gedanken material. Beyond studying the silicon multiple bonds in a crystal, we propose another method for protecting these very reactive bonds. We suggest that by isolating the triple bonds from each other in a crystal lattice with a large vacuum cavity separating them may serve as a sufficient barrier to allow construction of a metastable crystal containing silicon triple bonds. This metastable structure may be further stabilized by synthesis in a rare gas matrix allowing the inert gas to fill the interstitial regions. The highly reactive triple bonds would then be protected by being separated from each other and have a non-reactive barrier between them as well. Synthesis with the very reactive silicon triple bond may be challenging. Even if the synthesis of a crystal lattice can not be realized experimentally, we can provide insight into the character of silicon multiple bonds in the solid state by examining the properties of the crystal as a gedanken material.

We constructed a dilated diamond silicon triple bond crystal from the underlying motif suggested by the core of the silicon disilyne molecule. We relaxed this crystal structure and found that it is locally stable. Density function theory calculations using GGA-PBE pseudopotentials were used to find the local minimum for this lattice[30, 31, 28, 29, 39, 40]. Choosing the core portion of this molecule along with its tetrahedral bonding we constructed a dilated diamond lattice structure where the fundamental unit consisted of the triple bond present in the silicon disilyne molecule (See: Figure 3.2). This molecule was placed in an face-centered-cubic (FCC) lattice. The overall lattice can be viewed as a diamond lattice with five atoms in each tetrahedra bonding unit (half of the molecule). A diamond lattice provides us with the tetrahedral bonding that is compatible with the silicon disilyne core bonding geometry. In addition the most crucial feature of the diamond lattice is the open lattice structure allowing for a large separation between the silicon triple bonds. This large separation allows for a spatial isolation of

	Disylene Molecule	Dilated Diamond Silicon Lattice
Triple Bond Length	2.06 Å	2.16 Å, 2.18 Å
Triple Bond Angle	137.4°	131.6°-133.8°
Tetrahedral Bond Length		2.35Å-2.38Å
Tetrahedral Angles	106.4°-114.7°	99.2°-125.3°
Binding Energy		-3.96 eV/atom
Diamond Silicon	-5.325 eV/atom	2.35 Å

Table 3.1. Comparison of Structural Properties of the Silicon Triple Bond (Disylene) Molecule and the Dilated Diamond Silicon Lattice relaxed via DFT.

the triple bond from its surroundings without the use of the protective groups used in the molecule.

Comparing the geometry of the relaxed silicon dilated diamond structure with the geometry of the experimentally constructed molecule we find consistent results in bonding geometry (see table: 3.1.2). We see that the triple bonds are bent at an angle of 137° in the molecule. The angle of the triple bond is 180° in the analogous carbon structure. The triple bond is bent due to the weak π bonding between silicon atoms [66]. In all of our DFT calculations final structures are relaxed with an 8x8x8 grid of k-points with a high energy cutoff (1.3* EnMax), where EnMax is the maximum energy present in the pseudopotential. For the case of Silicon EnMax=245.3 with a cutoff energy of 318.9 eV. The high cutoff energy guarantees that absolute energies are converged to a few meV. Final ionic positions are relaxed via a conjugent gradient method to at least a tolerance of 0.05 eV/angstrom (0.001 eV/angstrom in most cases).

The dilated diamond silicon structure has a binding energy of -3.96 eV/atom which is 1.36 eV/atom above diamond silicon under zero external pressure. To give a scale for comparing this energy difference we can compare to typical energy scales for carbon. This is a large difference in energy as compared to the (.4eV/atom- .7eV/atom) increase in energy to form the C_{60} (buckyball structure) and similar structures [5] when comparing to graphite. This energy scale may not be directly applicable to silicon, but gives a guide for typical energy differences for commonly synthesized structures. This difference in energy could make this silicon crystal very challenging to construct experimentally. Nevertheless, analyzing the details of the characteristics of the triple bond provides useful insight into how silicon multiple bonds are formed from a theoretical standpoint.

3.1.3 Electronic Structure

Now we compare and contrast the silicon structure to the analogous carbon structure. The reason for comparing to the analogous carbon structure is because carbon has very strong triple bonds and are very well known. We can use the information we know about carbon to gain some insight into how multiple bonded silicon behaves differently. We calculated the band structure for our dilated silicon lattice and the analogous carbon lattice. As mentioned above, the triple bond in carbon forms a 180° angle, while the silicon structure has a bond angle 137°. The straight triple bond in carbon allows for a large overlap in the electronic orbitals providing the strong and well behaved carbon triple bonds. Looking at the band structure for carbon in figure 3.3 we see a cluster of eight bands (highlighted in red and blue). These highest eight occupied bands are formed primarily from the electrons responsible for the triple bonds. These bands are very flat and form a group of bands that is separated by more than five electron volts from the nearest level. The clustering of these bands indicates that the electrons in triple bonds stay localized to their bonds indicating a strong triple bond.

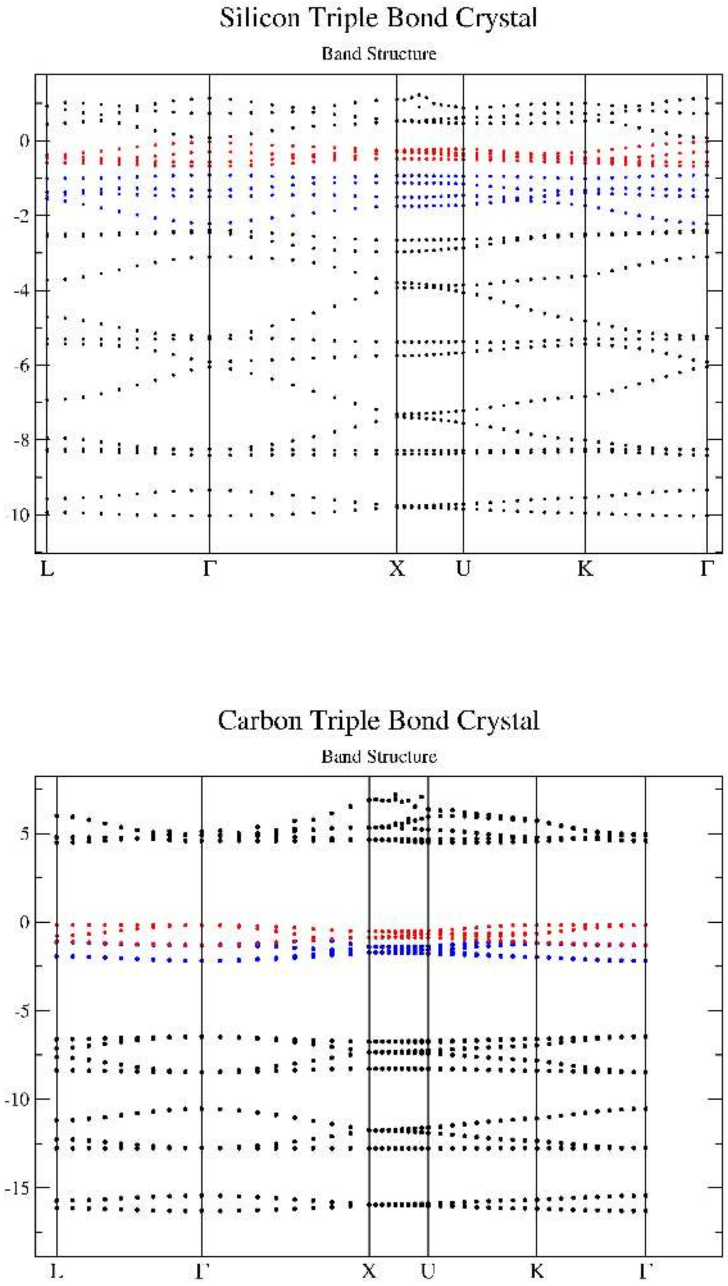

Fig. 3.3. Band structure plots for the silicon dilated diamond crystal lattice and the analogous carbon lattice.

Comparing the band structure for the dilated diamond silicon structure to the carbon band structure, we see the highest eight occupied bands spread out. The energy gap above and below (relative to the carbon band structure) shrinks significantly. This indicates much weaker π bonding in the triple bonds for silicon. The expanded energy range of these bands along with the smaller gap allows the electrons to be less localized in the triple bond region. In both the carbon and silicon crystal cases we have a band gap. For the carbon case the band gap is much larger. The dilated diamond silicon crystal lattice has a band gap of .1 eV while the analogous carbon structure has a band gap of 5 eV. Since the band gap is normally underestimated using GGA, the actual band gap in these structures would be expected to be larger. Synthesized versions of both of these crystals are likely to have a large enough band gap to be insulators.

Next we examine the band decomposition of the charge density for the eight highest occupied bands. The charge density plots for these bands gives us another way to examine the character of the triple bonds in each crystal.

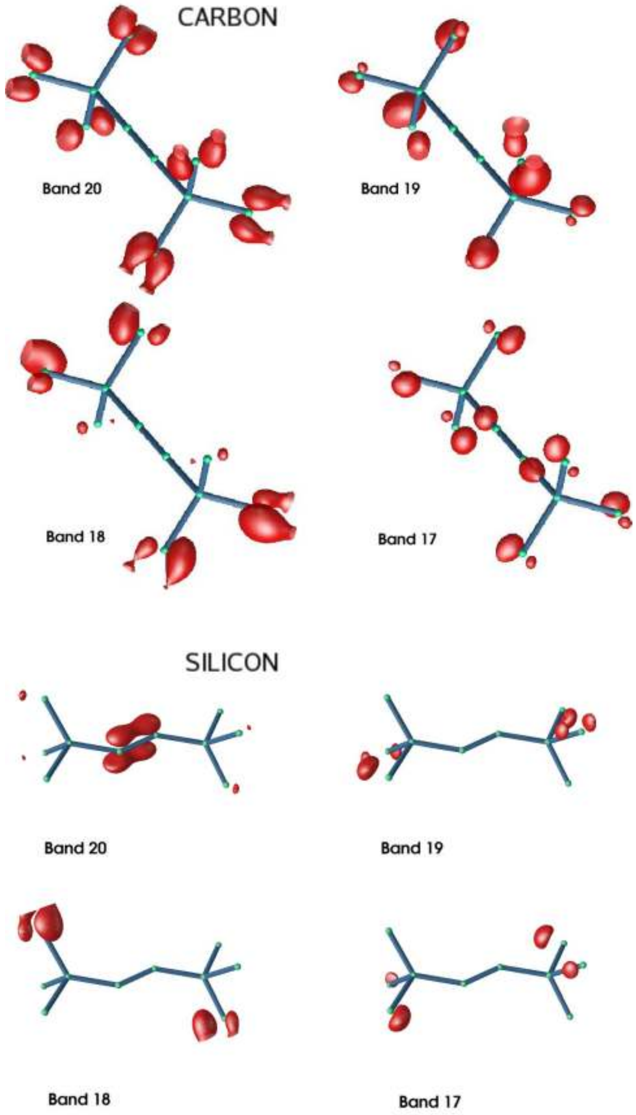

Fig. 3.4. Isosurface plot for the charge density of the dilated diamond silicon structure and analogous carbon structure bands 17-20.

The electron density for the highest eight occupied bands are shown in figures 3.4 and 3.5. In examining both charge density plots for the analogous carbon structure (figures 3.4 and 3.5) we see typical π bonding states for all bands. It is especially easy to see the π bonding character in the case of bands 15 and 16 in figure 3.4 for carbon, since that charge density is not split across the unit cell boundary. Comparing to the silicon version of the structure we see the typical π bonding orbitals when looking at band 18 and 20 in figure 3.4. In the other bands the orbitals do not appear to be similar to the π bonding in the carbon structure. Even in the case where the orbitals are recognizable as typical π bonds we can see that the charge is not distributed as uniformly in the silicon case as it appears in the carbon case. It is clear that the π bonding is much weaker in the silicon case than the carbon case as expected, contributing to the bent very reactive triple bond in our silicon crystal.

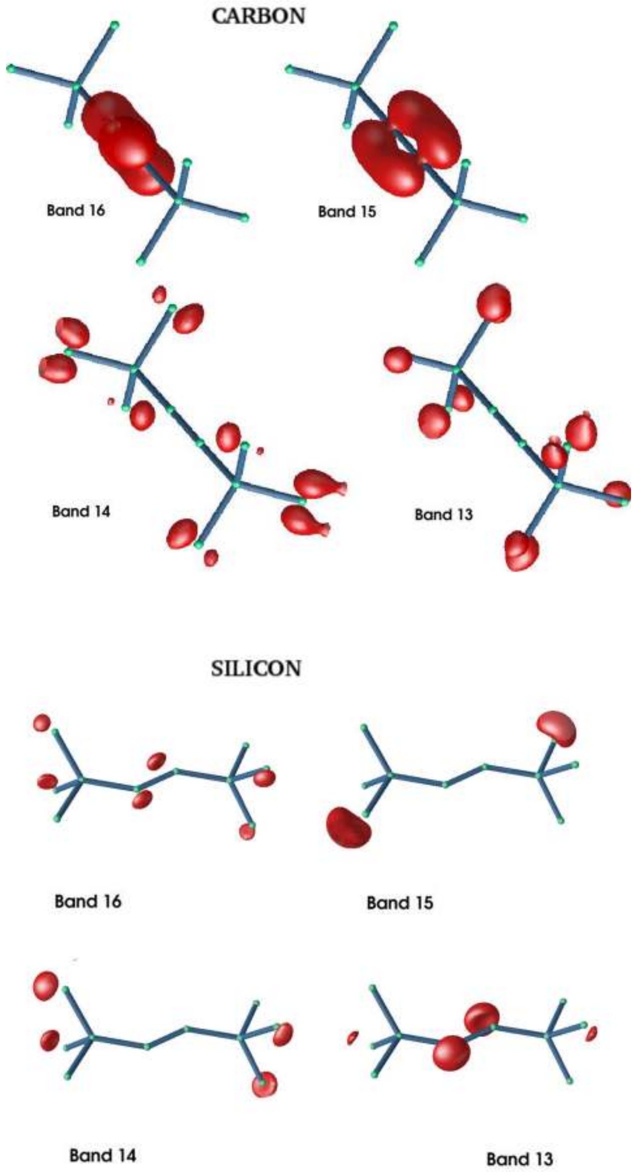

Fig. 3.5. Isosurface plot for the charge density of the dilated diamond silicon structure and analogous carbon structure bands 13-16.

Spin-polarized calculations were also performed to further examine the character of the triple bonds in the dilated diamond silicon structure. We would like to examine the possibility of any partial dangling bond character present in the structure, due to the weak π bonding. A state with dangling bond character has unpaired electrons which might lead to a spin-polarized ground state. In both the silicon and carbon case the spin-polarized calculation showed only very minor structural differences when comparing to the non-spin-polarized case. Examining the band structure of the analogous carbon system(figure 3.7) we see the wide gaps between clusters of bands very similar to the non-spin-polarized calculation. For the silicon case (figure 3.6) we see that the small band gap present in the non-spin polarized calculation disappears, and the clustering of the bands becomes slightly less apparent. The spin states of the electrons are found to be exactly degenerate in energy. This indicates that any weak partial dangling bond character that may be present does not generate spin polarization in the system.

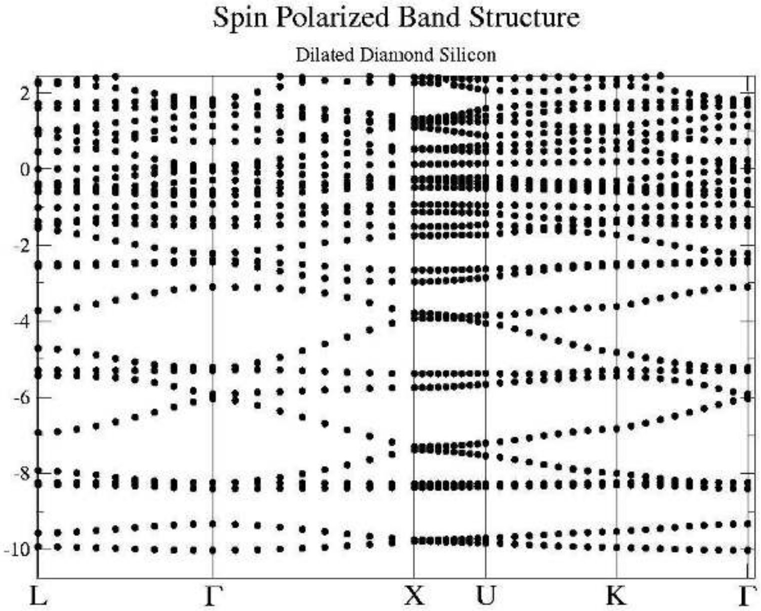

Fig. 3.6. Spin-polarized band structure silicon.

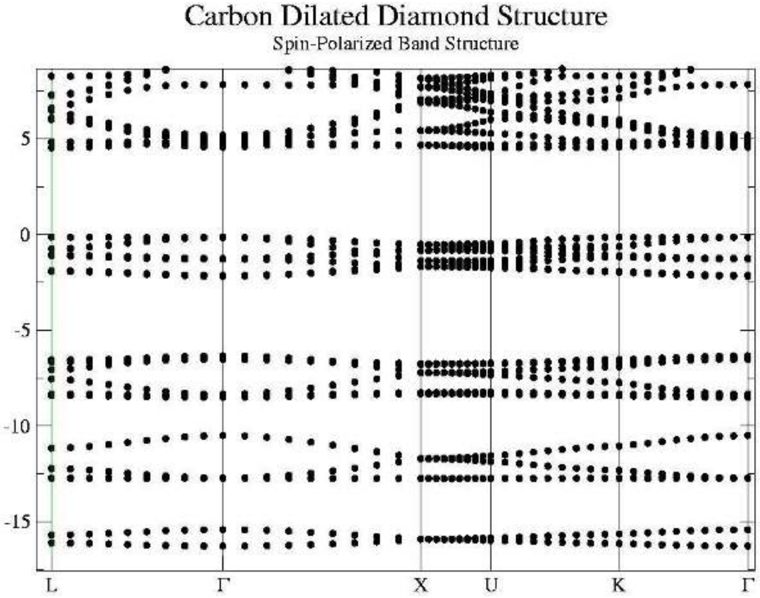

Fig. 3.7. Carbon spin-polarized band structure

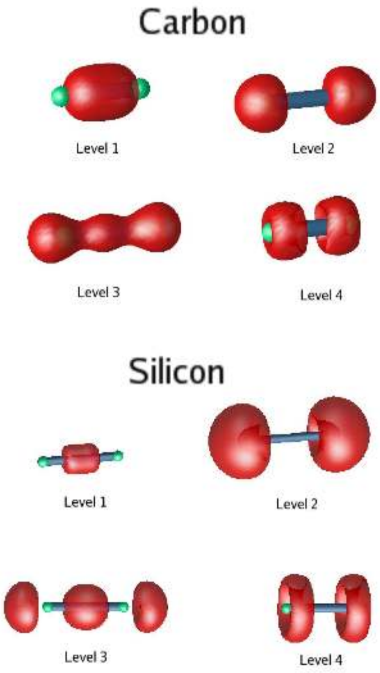

Fig. 3.8. Isolated carbon and silicon dimers: The figure above shows the much stronger preference for carbon to form multiple bonds than silicon. The lowest four energy levels are shown (lowest to highest: 1,2,3,4). Level 3 shows the most significant difference where there is a much stronger overlap in the case of the carbon dimer.

In both the band structure and the band decomposition of the charge density, we find evidence of the weak π binding in the silicon crystal structure. The overlapping of bands in the silicon band structure along with few π bonding characteristic orbitals in the charge density plots suggest a weak triple bond. However, π bonds do exist, and form bands in a distinct energy range. Comparing to the analogous carbon structure we see nice characteristic π bonding orbitals that indicate it is not the structure itself causing the weak binding. Silicon's weak bonding even causes the bond to be bent. This bent very reactive bond needs protection (spatial or physical) to avoid bonding to neighboring atoms.

3.1.4 Phonons

We examined the phonon spectrum to test the stability of the crystal lattice. Phonons can be used as a tool to examine stability because they give some information about the curvature of the energy surface when atoms in the crystal are displaced. If we consider the position of an atom in a crystal at time t $R^{'}(t)$ and R as the position in an undistorted crystal, we can define the atomic displacement $u(R,t)$ using the following relation:

$$R^{'}(t) = R + u(R,t). \tag{3.1}$$

Using the total potential energy as a function of the atomic displacements ($V(u)$), we can write the equations of motion as:

$$M\ddot{u}(R,t) = \frac{\delta V(u)}{\delta u(R,t)} \tag{3.2}$$

where M is the atomic mass. The potential energy can be expanded as a Taylor series in terms of the atomic displacements about the minimum energy positions.

$$V(u) = V_0 + \frac{1}{2} \sum_{R,R'} u(R,t) \cdot C(R,R') \cdot u(R',t) + O(u^3) \tag{3.3}$$

where

$$C(R,R') = \frac{\delta^2 V}{\delta u(r) \delta u(R')} \tag{3.4}$$

The term linear in u is not present due to opposing vanishing forces on the atoms. The constance C(R,R') are atomic force constants connected to each other by the symmetry of the crystal. Since there is translational invariance these constance only depend on $R{-}R'$. Using the harmonic approximation (i.e. ignoring $O(u^3)$ and higher) our equations of motion are:

$$M\ddot{u}(R,t) = -\sum_{R'} C(R-R') \cdot u(R',t) \tag{3.5}$$

Since we have translational invariance, our solution must be a Bloch wave solution:

$$u(R,t) = \frac{1}{\sqrt{M}} \omega e^{iq \cdot R - i\omega t} \tag{3.6}$$

Introducing the following discrete Fourier transform:

$$D(q) = \frac{1}{M} \sum_{R} e^{-iq \cdot R} C(R) \tag{3.7}$$

and by substuting in the Bloch relation we obtain the following relationship:

$$D(q) \cdot \omega = \omega^2 \omega \tag{3.8}$$

The matrix defined by equation 3.8 is known as the dynamical matrix. There are $3N$ solutions to this eigenvalue problem for each $\mathbf{q}$ in the Brillouin zone. These solutions $\omega_j(q)$ are the phonon dispersion relations. We used the frozen phonon method to calculate the phonon frequencies. Each atom is displaced in two locations along each degree of freedom. The energy of the system with each displacement is calculated. A dynamical matrix (Hessian matrix) is constructed from these energies, where the eigenvalues of the matrix are the phonon frequencies and the eigenvectors represent the atomic displacements of the mode[38].

The phonon frequencies were examined along with the corresponding eigenvectors at γ point (q=0). We found several low energy phonons. The lowest energy phonon (2.21 meV), is an azimuthal rotation of the triple bond atoms around the axis between their neighboring sp^3 bonded atoms. This is a low energy mode, which is common among similar buckled bond structures such as quartz [4, 10, 55, 53, 36]. The other low energy modes mainly involve the triple bond atoms in a vibrational motion that is radially relative to the axis connecting the sp^3 atoms. The phonon modes can be interpreted as an indication that the triple bonds can be easily bent. This bending of the the very reactive triple bonds makes it difficult to protect the triple bonded atoms from bonding to additional neighbors.

Performing an ab-initio molecular dynamics simulation for the dilated diamond silicon structure confirms that the motion of the triple bonded silicon atoms is primarily responsible for the short lifetime of this structure. We performed a molecular dynamics simulation with a constant temperature of 600K. A high temperature was chosen in order to gain some realistic insight into how stable the silicon structure might be. We are restricted to simulation times of 2 ps maximum due to computational constraints. The increased temperature provides an artificial way to test the activation barrier height for a longer effective time at a lower temperature. If the crystal is stable for 2 ps at 600 K, it is more likely to be stable for a more realistic time at a lower temperature. The simulation shows the crystal falls apart after 0.5 ps. Two of the silicon atoms in neighboring triple bonds eventually bond to each other. The motion of the triple bonded atoms allows the crystal structure to fall apart as we might guess from looking at the lowest energy phonon mode. All of the low energy phonon modes involve primarily motion among the very reactive triple bonded atoms.

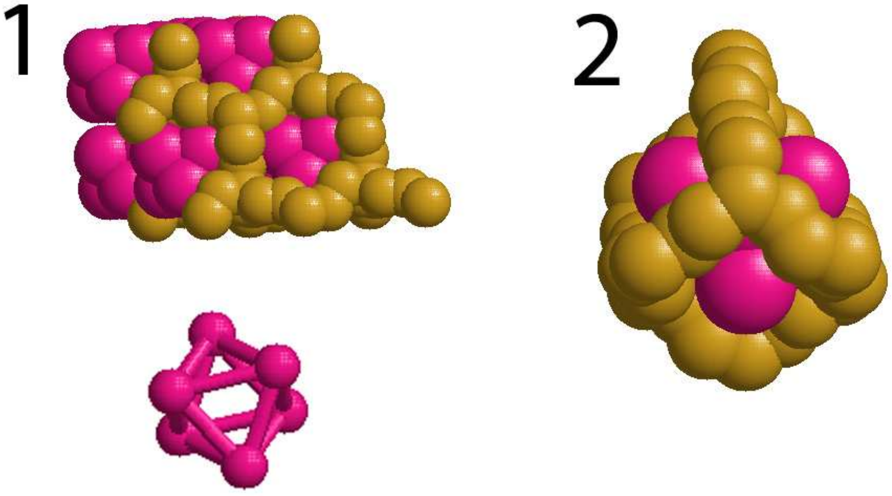

Fig. 3.9. Space-filling model representation for the resulting relaxed silicon lattice structure with rare gas atoms inserted in the opening to serve as a physical barrier in addition to the spatial barrier already present in the structure. 1) Six argon atoms in the interstitial region form and octahedron to fill the space. 2) Eight argon atoms filling the interstitial region.

We hope to hinder the motion of these triple bonded atoms by filling the vacuum cavity between triple bonds with rare gas atoms to lengthen the lifetime of the crystal. This is a method commonly used in chemistry to help stabilize reactive compounds [13, 24]. The target case is to find the gas that will fill the interstitial region with a small increase in the overall energy, when comparing to sum of the energy of the rare gas and the silicon lattice calculated separately. This small increase in energy is desirable as an indication that the silicon atoms in the triple bonds are feeling some repulsion from the inert gases. The inert gases are chosen as a way to provide a non-interacting physical barrier between silicon triple bonds. We begin by inserting four argon atoms (3.3 Åbond length in solid argon at zero pressure). The argon was arranged in a tetrahedral configuration to match the tetrahedral symmetry of the interstitial region. This configuration was relaxed and we found a small decrease in the total system energy.

We increased to six argon atoms in an octahdral configuration with no increase in the crystal's energy. Examining the new phonon frequencies, we find only small changes in the frequencies. A molecular dynamics simulation confirms that the six argon atoms are not a sufficient barrier to prevent the crystal structure from falling apart. By increasing the size of the atom (and number of atoms) inserted into the interstitial region we hope to increase the physical barrier between the triple bonded silicon atoms while finding only a small increase in the overall system energy. The six argon atom case clearly does a better job filling the interstitial region. The octehdron has the same rotational symmetry as a tetrahedron, but the rings formed by the triple bonds have a large hole in their center. This hold suggests that adding more atoms may be preferable.

Adding eight argon atoms in an initial cubic configuration to the interstitial region in the triple bond cage, we also find a small decrease in energy of the system, when compared to their individual parts. The argon atoms do fill the space more efficiently and have a symmetry consistent with the tetrahedral symmetry of the interstitial opening. The eight argon atoms form a cluster with a tetrahedral core with the additional four atoms close packed in the center of each face of the tetrahedron. The phonon modes calculated for this configuration again had several low energy modes. Performing a molecular dynamics simulation of the configuration with eight argon atoms shows the does not have an increased lifetime falling apart after .2 ps. The same mechanism is responsible for the structure falling apart with the triple bond atoms in neighboring chains bonding to each other. Inserting krypton a slightly larger rare gas atom gives the same relaxed structure in both cases (6 atoms and 8 atoms). A molecular dynamics simulation of this case show the same result as argon with the structure falling apart after 0.3 ps. The next rare gas atom (xenon) is too large and can not fit inside the opening for the six or eight atom case causing the silicon bonds to break. Applying a pressure to increase the number of rare gas atoms in the cavity will likely cause the silicon bonds to break in a similar manner to inserting extra xenon atoms. Overall the insertion of a single rare gas inside the cavity of the dilated diamond silicon structure does not improve the stability of the structure.

We demonstrated the first crystal structure which integrates a silicon triple bond. The motion of the triple bond atoms in the structure due to the soft phonon modes are responsible for the instability of the structure. Creating a physical barrier in addition to the spatial barrier built into the lattice by inserting a rare gas in the interstitial opening is not yet sufficient to stabilize the structure. A physical barrier would have to be present in the corners of the opening to prevent the atoms in neighboring chains from bonding together. When inserting a single rare gas into the opening tightly packed isocahedra form, filling the center of each ring between neighboring interstitial regions. Possibly a mixture of rare gases may be able to fill the void in the corner of the interstitial region. Since eight krypton atoms efficiently fill the larger holes in the region, a few smaller atoms (helium or neon) may be able to fill the void in the corners. We provided a detailed analysis of this novel form of silicon involving a triple bond in a crystal form. We find results consistent with the molecular case. The crystal structure is metastable and will need to be very cleverly synthesized in order to overcome the reactivity of the triple bonds. Synthesis in a rare gas mixture of krypton and neon or helium may provide the environment necessary for synthesis. In addition, knowledge about the bonding character of silicon triple bonds provides insight into possible compounds that silicon may form. For example, the bands formed by triple bonds to silicon in alloys are likely to be very broad and overlap, when compared to a similar carbon structure. Therefore, independet of success in overcoming synthesis obstacles the dilated diamond silicon structure has a significant value as a gedanken material.

3.2 Hybrid sp^2 - sp^3 Silicon Structure

Using the same methodology as in the creation of the dilated diamond silicon structure. We created a crystal lattice containing a silicon double bond out of the bonding geometry from the core of a recently synthesized molecule. In this molecule (figure 3.10), the reactive silicon double bond is again protected by bulky protective groups. In the trisilaallene molecule the central silicon atom with two double bonds has four noted locations in the molecule. These locations are noted in the figure as A-D. The experimental population of each location is given as 53%,22%,19%, and 7% at -50°,respectively [20]. As the temperature decreases the population of the states of the central atom become more uniform.

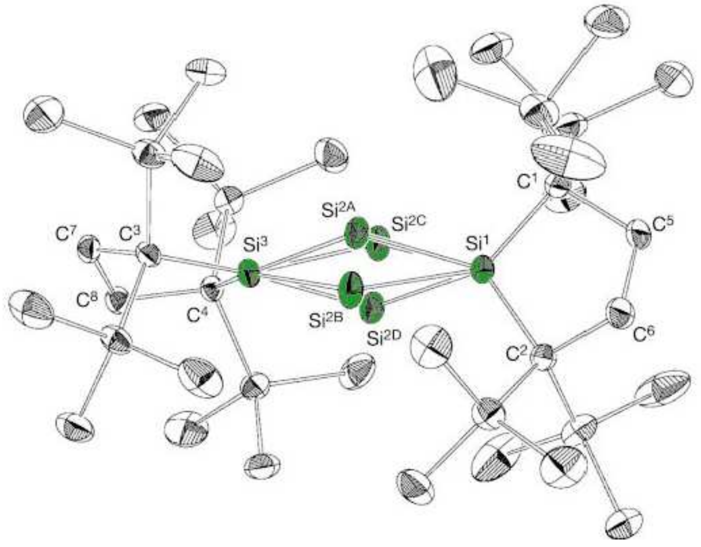

Fig. 3.10. Trisilaallene molecule with an sp-hybridized silicon atom in the center. The sp-hybridized atom has four locations experimentally labelled A-D and are populated at 53%,22%,19%, and 7% at -50° C, respectively [20].

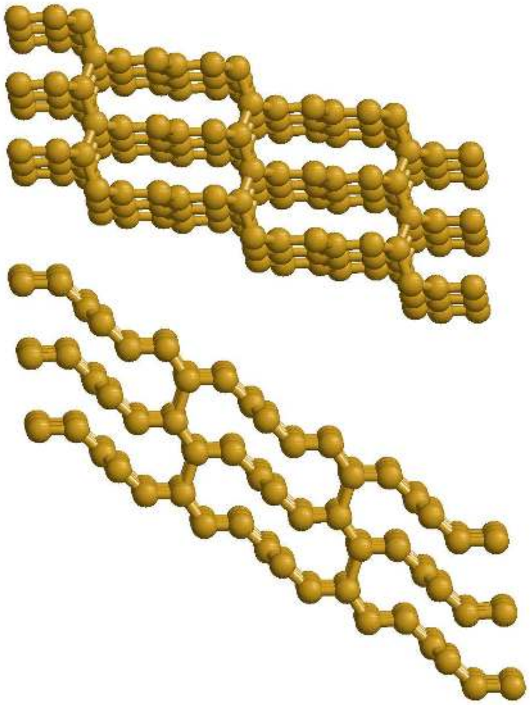

Fig. 3.11. Initial crystal lattice constructed with the core from the trisilaallene molecule (top and side view)

We used the core region of this molecule consisting of the sp-hybridized atom and its two neighbors. This unit was stitched into a crystal lattice depicted in figure 3.11. As in the triple bond case, the initial crystal structure was constructed to create a large gap between neighboring double bonded atoms. We then relaxed this structure using DFT and the PAW-PBE pseudopotentials used in the triple bond case. The crystal structure was found to be unstable. The floppy positioning of the central atom allows the crystal to collapse. However, the resulting structure proved to be interesting as a possible transitional material between diamond and graphitic silicon and may be further stabilized under negative pressure.

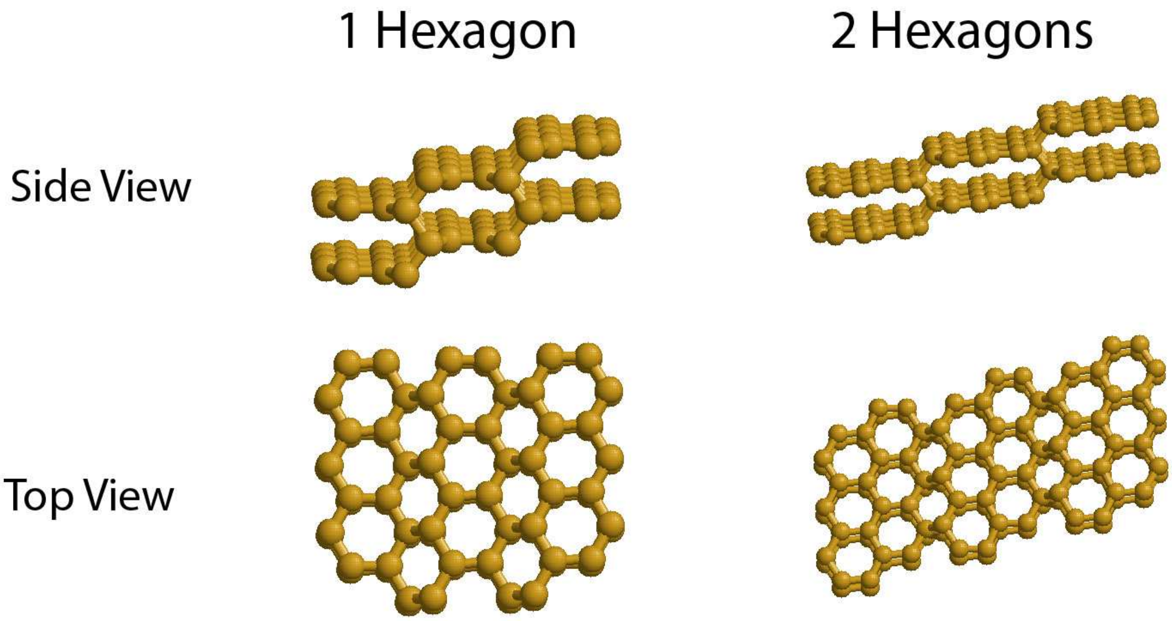

Fig. 3.12. Relaxed structure containing sp^3 and sp^2 silicon bonds. The structure is made of staggered ribbons of graphitic silicon with sp^3 atoms linking the layers. Shown are the versions of the structure with ribbons of width 1 and 2 hexagons.

	One-hexagon Gallery	Two-hexagon Gallery
Basis Vector 1	(-3.96,0.02,-3.73)	(0.00,0.04,-3.74)
Basis Vector 2	(-1.98,1.18,-3.73)	(-1.99,1.24,-3.74)
Basis Vector 3	(-1.98,3.39,-3.73)	(-1.99,3.48,-3.74)
Basis Vector 4	(-3.96,4.55,-3.73)	(0.00,4.57,-3.74)
Basis Vector 5		(0.00,6.80,-3.74)
Basis Vector 6		(-1.99,8.01,-3.74)
Lattice Vector 1	(-3.97,0.00,0.000)	(-3.98,0.00,0.00)
Lattice Vector 2	(0.00,5.91,-1.86)	(1.99,9.38,-1.87)
Lattice Vector 3	(0.00,0.00,-3.73)	(0.00,0.00,-3.74)

Table 3.2. Lattice vectors and basis vectors for the relaxed $sp^2 - sp^3$ hybrid "gallery" structures shown in figure 3.12 (All units are in angstroms).

The resulting locally stable form of silcon, integrates sp^2 and sp^3 atoms into a family of structures. This family of silicon structures is composed of ribbons of graphitic silicon with a wall of sp^3 silicon atoms connecting the ribbons in a staggered pattern (figure 3.12). The binding energy of the single hexagon structure was calculated as 5.01 eV/atom(compared to the initial structure 4.72 eV/atom), 0.315 eV above diamond silicon and 1.05 eV below the dilated diamond silicon structure. The binding energy of the two and three hexagon cases go down only slightly with binding energies of 4.95 eV/atom and 4.91 eV/atom respectively. Graphitic silicon is predicted to be locally stable. Graphitic silicon is expected to be further stabilized to an experimentally practical level at high negative pressure (-69 kbar) [66]. This family of structures provides a locally stable transitional structure between standard diamond silicon and graphitic silicon. The family of structures can be extended by increasing the width of the graphitic ribbon between the sp^3 silicon atoms. Increasing the number of hexagons in the ribbon should give results more similar to graphitic silicon as the ribbons turn into larger graphitic silicon sheets.

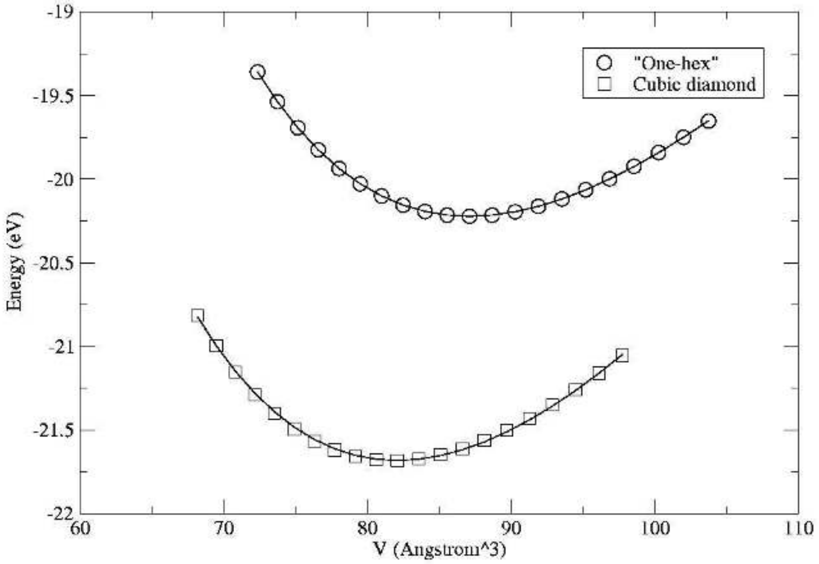

Fig. 3.13. Energy versus volume curves for diamond silicon at the single hexagon ribbon structure depicted in figure 3.12

Due to the weak interaction between graphitic silicon layers, we would expect the direction perpendicular to the hexagons (z-direction) to be the softest direction. Examining the energy-volume curves, we can see that the single hexagon structure is softer than diamond silicon due to the wider shaped curve, because of the weak interaction between layers.

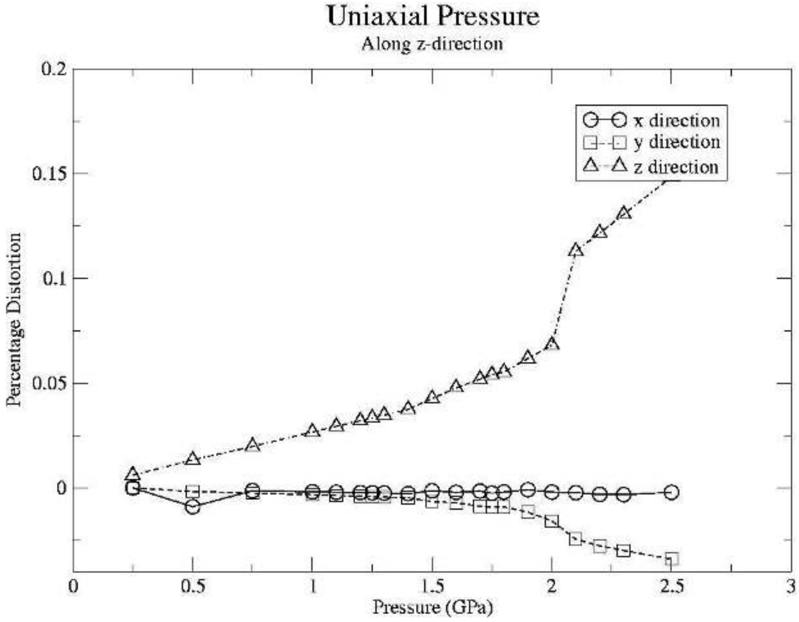

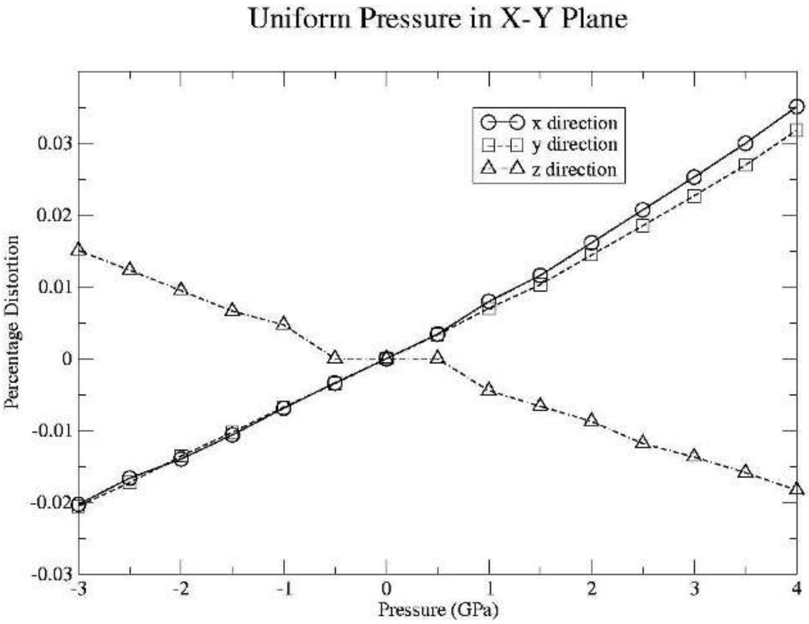

Fig. 3.14. Distortion under negative pressure along the z-axis (perpendicular to the graphitic ribbons) (top). Distortion under uniform pressure along the x-y plane (in the plane of the graphitic ribbons) (bottom).

We can see from figure 3.14 that the distortion of the crystal lattice is large along the z-axis under unixial pressure. Along the x and y direction there is only a small distortion until we reach higher pressures (1.5 GPa). These results indicate that the lattice is much easier to stretch along the z-axis, due to the weak inter-layer bonding of the ribbons. While along the x and y directions the sp^2 silicon atoms provide a relatively stiff framework.

Another possible new form of silicon has been found. The lattice is much easier to stretch along one direction. This indicates that the structure may be preferred to diamond silicon under a high uniaxial stress. Previous research predicts that graphitic silicon may be plausable under negative pressure [66]. The structure presented here is a natural transition structure that may allow graphitic silicon to be formed. Adding additional hexagons to each ribbon leads the structure to a more graphitic like structure, and there is a natural path under which the structures could transition from one to another. If you break one set of sp^3 bonds by cutting the bonds the resulting structure consists of a distorted ribbon structure with 2n+1 hexagons. Under negative pressure you would expect the distorted region of the ribbon (previously sp^3 region) to straighten out. In addition to being a plausable metastable structure that could act as a transitional structure to graphitic silicon. This family of silicon structures that combines sp^2 and sp^3 silicon bonds may open the door to new silicon cage-like or ring structures (for example:where the ribbon portion of the structure is wrapped into a ring). Therefore, the analysis of this hybrid structure could be very important in analyzing the feasability of new hybrid sp^2-sp^3 silicon structures.

References

[1] P. Bartlett, R. H. Ottewill, and P. N. Pusey. Superlattice formation in binary-mixtures of hard-sphere colloids. *Physical Review Letters*, 68:3801–3804, 1992.

[2] V. E. Bazterra, M. B. Ferraro, and J. C. Facelli. Modified genetic algorithm to model crystal structures. i. benzene, naphthalene and anthracene. *Journal of Chemical Physics*, 116:5984–5991, 2002.

[3] V. E. Bazterra, M. B. Ferraro, and J. C. Facelli. Modified genetic algorithm to model crystal structures. ii. determination of a polymorphic structure of benzene using enthalpy minimization. *Journal of Chemical Physics*, 116:5992–5995, 2002.

[4] N. Binggeli, N. R. Keskar, and J. R. Chelikowsky. Pressure-induced amorphization, elastic instability, and soft modes in α-quartz. *Physical Review B*, 49:3075–3081, 1994.

[5] J. R. Chelikowsky. Nucleation of c_{60} clusters. *Physical Review Letters*, 67(21):2970–2973, 1991.

[6] X. Cottin and P. A. Monson. Substitutionally ordered solid-solutions of hard-spheres. *Journal of Chemical Physics*, 102:3354–3360, 1995.

[7] D. Deaven and K. M. Ho. Molecular-geometry optimization with a genetic algorithm. *Physical Review Letters*, 75:288–291, 1995.

[8] T. Douglas and M. Young. Virus particles as templates for materials synthesis. *Advanced Materials*, 11:679–685, 1999.

[9] R. M. Dreizler and E. K Gross. *Density Functional Theory*. Springer-Verlag, Berlin, 1990.

[10] W. Dultz, M. Quillichini, and J. F. Scott. Phonon spectra of quartz isomorphs. *Physical Review B*, 11:1648–1653, 1975.

[11] M. Fialkowski, A. Bitner, and B. A. Grzybowski. Self-assembly of polymeric microsphers of complex internal structures. *Nature Materials*, 4:93–97, 2005.

[12] M. S. Gordon and J. A. Pople. Structure and stability of a silicon-carbon triple bond. *Journal of Chemical Physics*, 103(11):2945–2947, 1981.

[13] H. H. Guenthard, T. K. Ha, and R. Gunde. Static and dynamic aspects of matrix isolated molecules: are molecules isolated in rare gas matrices really force free? *Journal of Molecular Structure*, 217:143–150, 1990.

[14] S. Hachisu and S. Yoshimura. Optical demonstration of crystalline superstructures in binary mixtures of latex globules. *Nature*, 283:188–189, 1980.

[15] S. Hachisu and S. Yoshimura. *Physics of Complex and Supermolecular Fluids*. Wiley, New York, 1987.

[16] K. M. Ho, A. A. Shvartsburg, B. Pan, Z. Lu, C. Wang, J. Wacker, J. Fye, and M. Jarrold. Structures of medium-sized silicon clusters. *Nature*, 392:582–585, 1998.

[17] P. Hohenberg and W. Kohn. Inhomogeneous electron gas. *Physical Review B*, 136:B864–B871, 1964.

[18] John H. Holland. *Adaptation in Natural and Artificial Systems.* University of Michigan Press, Ann Arbor, Michigan, 1975.

[19] N. Hunt, R. Jardine, and P. Bartlett. Superlattice formation in mixtures of hard-sphere colloids. *Physical Review E*, 62(1):900–913, 2000.

[20] S. Ishida, T. Iwamoto, and M. Kira. A stable silicon-based allene analogue with a formall sp-hybridized silicon atom. *Nature*, 421:725–727, 2003.

[21] P. Jiang, J. F. Bertone, and V. L. Colvin. A lost-wax approach to monodisperse colloids and their crystals. *Science*, 291:453–457, 2001.

[22] S. A. Johnson, P. J. Ollivier, and T. E. Mallouk. Ordered mesoporous polymers of tunable pore size from colloidal silica templates. *Science*, 283:963–965, 1999.

[23] R. O. Jones and O. Gunnarsson. The density functional formalism, its applications and prospects. *Review of Modern Physics*, 61:689–746, 1989.

[24] L. Kim, W. Xuefeng, L. Manceron, and L. Andrews. Absorbtion spectra of ground stte low-lying electronic states of copper nitrosyl: a rare gas matrix isolation study. *Journal of Physical Chemistry A*, 109:10264–10272, 2005.

[25] K. Kobayashi, N. Takagi, and S. Nagase. Do bulky aryl groups make stable silicon-silicon triple bonds synthetically accessible? *Organometallics*, 20:234–236, 2001.

[26] W. Kohn and L. J. Sham. Self-consisten equations including exchange and correlation effects. *Physical Review A*, 140:A1133–A1138, 1965.

[27] John Koza. *Genetic Programming: On the Programming of Coputers by Means of Natural Selection.* Wiley, New York, 1992.

[28] G. Kresse and J. Furthmueller. Efficiency of ab-initio total energy calculations for metals and semiconductors using a plane-wave basis set. *Computational Meterial Science*, 6:15–50, 1996.

[29] G. Kresse and J. Furthmueller. Efficient iterative schemes for ab initio total-energy calculations using a plane-wave basis set. *Physical Review B*, 54:11169–11186, 1996.

[30] G. Kresse and J. Hafner. Ab initio molecular dynamics for liquid metals. *Physical Review B*, 47:558–561, 1993.

[31] G. Kresse and J. Hafner. Ab initio molecular-dynamics dimulation of the liquid-metal amorphous semiconductor transition in germanium. *Physical Review B*, 49:14251–14269, 1994.

[32] L. Lapidus and G. F. Pinder. *Numerical Solutions of Partial Differential Equations in Science and Engineering.* John Wiley & Sons, New York, 1982.

[33] M. E. Leunissen, C. G. Christova, A. Hynninen, C. P. Royall, A. I. Campbell, A. Imhof, M. Dijkstra, R. van Roij, and A. van Blaaderen. Ionic colloidal crystals of oppositely charged particles. *Science*, 437:235–240, 2005.

[34] J. R. Morris, D. M. Deaven, and K. M. Ho. Genetic-algorithm energy minimization for point charges on a sphere. *Physical Review B*, 53:R1740–R1743, 1996.

[35] C. B. Murray, C. R. Kagan, and M. G. Bawendi. Synthesis and characterization of monodisperse nanocrystals and close-packed nanocrystal assemblies. *Annual Review of Material Science*, 30:545–610, 2000.

[36] R. Nava and R. Oentrich. Effects of low-lying phonon modes on the anomalous temperature dependence of the elastic constants of rutile and quartz. *J. Phys. Chem. Solids*, 59(1):135–140, 1998.

[37] R. G. Parr and W. Yank. *Density Functional Theory of Atoms and Molecules.* Oxford, New York, 1989.

[38] Pasquale Pavone. Old and new aspects in lattice-dynamical theory. *Journal of Physics: Condensed Matter*, 13:7593–7610, 2001.

[39] J. P. Perdew, K. Burke, and M. Ernzerhof. Generalized gradient approximation made simple. *Physical Review Letters*, 77:3865–3868, 1996.

[40] J. P. Perdew, K. Burke, and M. Ernzerhof. Generalized gradient appriximation made simple. *Physical Review Letters*, 78:1396, 1997.

[41] J. P. Perdew, K. Burke, and Y. Wang. Generalized gradient approximation for the exchange correlaction hole of a many-electron system. *Physical Review B*, 54:16533–16539, 1996.

[42] J. P. Perdew and Y. Wang. Accurate and simple analytic representation of the electron-gas correlation energy. *Physical Review B*, 45:13244–13249, 1992.

[43] W. H. Press, S. A. Teukolsky, W. T. Vetterling, and B. P. Flannery. *Numerical Recipes in C: The Art of Scientific Computing*. Cambridge University Press, New York, 1988.

[44] P. N. Pusey and W. van Megen. Phase-behavior of concentrated suspensions of nearly hard colloidal spheres. *Nature*, 320:340–342, 1986.

[45] F. X. Redl, K. S. Cho, C. B. Murray, and S. O'Brien. Three-dimensional binary superlattices of magnetic nanocrystals and semiconductor quantum dots. *Nature*, 423:968–971, 2003.

[46] R. Rengarajan, P. Jiang, D. C. Larrabee, V. L. Colvin, and M. Mittlemen. Colloidal photonic superlattices. *Physical Review B*, 64:205103–1 – 205103–4, 2001.

[47] J. V. Sanders. Close-packed structures of spheres of two different sizes, i. observations on natural opal. *Philosophical Magazine A*, 42:705–720, 1980.

[48] J. V. Sanders. Close-packed structures of spheres of two different sizes, ii. observations on natural opal. *Philosophical Magazine A*, 42:721–740, 1980.

[49] A. B. Schofield. Binary hard-sphere crystals with the cesium chloride structure. *Physical Review E*, 64:051403–1 – 051403–4, 2001.

[50] A. Sekiguchi, R. Kinjo, and M. Ichinohe. A stable compound containing a silicon-silicon triple bond. *Science*, 305:1754–1757, 2004.

[51] E. V. Shevchenko, D. V. Talapin, N. A. Kotov, S. O'Brien, and C. B. Murray. Structural diversity in binary nanoparticle superlattices. *Nature*, 439:55–59, 2006.

[52] J.C. Slater. The theory of complex spectra. *Physical Review*, 34:1293–1322, 1929.

[53] M. B. Smirnov. Lattice dynamics and thermal expansion of quartz. *Physical Review B*, 59(6):4036–4043, 1999.

[54] T. C. Smith, L. Haiyang, D. J. Clouthier, C. T. Kingston, and A. J. Merer. The electronic spectrum of silicon methylidyne (sich), a molecule with a silicon-carbon triple bond in the excited state. *Journal of Chemical Physics*, 112(8):3662–3670, 2000.

[55] Y. Tezuka, S. Shin, and M. Ishigame. Observation of the silent soft phonon in β-quartz by means of hyper-raman scattering. *Physical Review Letters*, 66(11):2356–2359, 1991.

[56] A. van Blaaderen. Colloids get complex. *Nature*, 439:545–546, 2006.

[57] K. P. Velikov, C. G. Christova, R. P. Dullens, and A. van Blaaderen. Layer-by-layer growth of binary colloidal crystals. *Science*, 296:106–109, 2002.

[58] Y. A. Vlasov, V. N. Astratov, and A. V. Baryshev. Manifestation of intrinsic defects in optical properties of self-organized opal photonic crystals. *Physical Review E*, 61:5784–5793, 2000.

[59] Michael D. Vose. *The Simple Genetic Algorithm: Foundations and Theory.* MIT Press, Cambridge, M.A., 1999.

[60] A. F. Wells. *Structural Inorganic Chemistry*. Oxford University Press, Oxford, 1984.

[61] R. West. Japan bats a triple. *Science*, 305:1724–1725, 2004.

[62] D. Whitley, S. Rana, and R. B. Heckendorn. The island model genetic algorithm: on separability, population size and convergence. *Journal of Computing and Information Technology*, 85:245–276, 1999.

[63] D. H. Wolpert and W. G. Macready. No free lunch theorems for search. *Technical Report SFI-TR-95*, 1995.

[64] D. H. Wolpert and W. G. Macready. No free lunch theorems of optimization. *IEEE Transactions on Evolutionary Computation*, 1:67–82, 1997.

[65] H. Wu, V. R. Thalladi, S. Whitesides, and G. M. Whitesides. Using hierarchical self-assembly to form three-dimensional lattices of spheres. *Journal of the American Chemical Society*, 124:14495–14502, 2002.

[66] M. T. Yin and M. L. Cohen. Structural theory of graphite and graphitic silicon. *Physical Review B*, 29:6996–6998, 1984.

[67] Y. Yin, Y. Lu, B. Gates, and Y. Xia. Template-assisted self-assembly: A practical route to complex aggregates of monodispersed colloids with well-defined sizes, shapes, and structures. *Journal of the American Chemical Society*, 123:8718–8729, 2001.

[68] Y. Yin, Y. Lu, and Y. Xia. A self-assembly approach to the formation of asymmetric dimers from monodispersed spherical colloids. *Journal of the American Chemical Society*, 123:771–772, 2001.

[69] C. C. Yun, J. L. Major, G. F. Strouse, R. Leon, R. Noetzel, S. Fafared, and D. Huffaker. Assembly of nanomaterials using bio-scaffolding. *Materials Research Society Symposium Proceedings*, 642:J2.3, 2001.

[70] Z. Zhang, A. S. Keys, T. Chen, and S. C. Glotzer. Self-assembly of patchy particles into diamond structures through molecular mimicry. *Langmuir*, pages 11547–11551, 2005.

Vita

Education

2006	Ph.D. , Condensed Matter Physics, The Pennsylvania State University
1999	M.S. ,Condensed Matter Physics, Iowa State University
1996	B.S. , Physics, Carnegie Mellon University